Mechanical Properties of Single Molecules and Polymer Aggregates

R. Berger, K. Binder, G. Diezemann, J. Gauss, M. Helm, H.-P. Hsu, A. Janshoff, T. Metzroth, I. Mey, A. Milchev, W. Paul, V.G. Rostiashvili, and T.A. Vilgis

Abstract This chapter deals with the mechanical properties of single polymer chains, aggregates, and supramolecular complexes. The topics discussed cover a broad range from fundamental statistical mechanics of the equilibrium elastic properties of single polymer chains to details of the behavior of binding pockets in

R. Berger, V.G. Rostiashvili, and T.A. Vilgis
Max-Planck-Institut für Polymerforschung, Ackermannweg 10, 55128 Mainz, Germany

K. Binder, and H.-P. Hsu
Institut für Physik, Johannes Gutenberg Universität Mainz, Staudinger Weg 7, 55128 Mainz, Germany

G. Diezemann (✉), J. Gauss, and T. Metzroth
Institut für Physikalische Chemie, Johannes Gutenberg Universität Mainz, Duesbergweg 10-14, 55128 Mainz, Germany
e-mail: diezemann@uni-mainz.de

M. Helm
Institut für Pharmazie und Biochemie, Johannes Gutenberg Universität Mainz, Staudinger Weg 5, 55128 Mainz, Germany

A. Janshoff, and I. Mey
Institut für Physikalische Chemie, Johannes Gutenberg Universität Mainz, Duesbergweg 10-14, 55128 Mainz, Germany

Institut für Physikalische Chemie, Tammannstraße 6, 37077 Göttingen, Germany

A. Milchev
Institut für Physik, Johannes Gutenberg Universität Mainz, Staudinger Weg 7, 55128 Mainz, Germany

Institute for Physical Chemistry, Academy of Sciences, Sofia 1113, Bulgaria

W. Paul
Institut für Physik, Johannes Gutenberg Universität Mainz, Staudinger Weg 7, 55128 Mainz, Germany
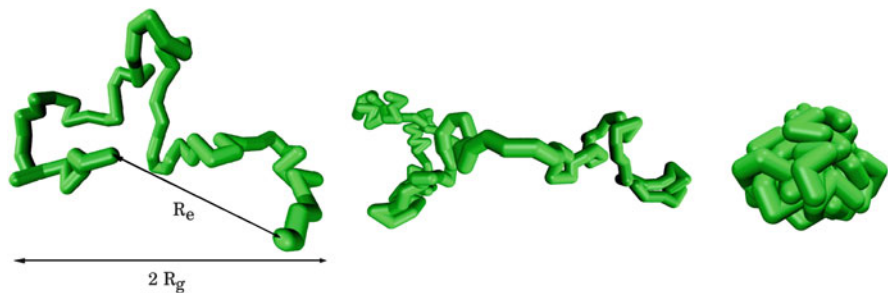
Institut für Physik, Martin Luther Universität Halle, 06099 Halle, Germany

biomolecular assemblies as observed by force spectroscopy. The first section treats the equilibrium mechanical properties of single polymer chains in various environments, investigated via extensive simulations employing coarse-grained models that have proven extremely successful in many branches of polymer physics, namely the bond-fluctuation model and the self-avoiding walk model. Apart from the phase behavior and the adsorption properties, the mechanical pulling of a polymer chain from a surface has also been investigated. Molecular dynamics (MD) simulations of spring-bead models and analytical theory are used to describe the stochastic dynamics of the system. After these sections treating fundamental aspects of mechanical adsorption and translocation of polymer chains, we consider the adhesion of specific molecular systems to form networks of hydrogen bonds. In particular, we discuss all-atom force probe MD simulations of calixarene catenane systems, which have recently been synthesized. These simulations have been performed in close collaboration with corresponding experimental investigations utilizing atomic force spectroscopy (AFS) on the same systems, which will be reviewed together with other experimental determinations of the mechanical properties of supramolecular assemblies. Although these investigations can give insight into the reversible dynamics of hydrogen-bond networks, AFS can also be used in order to determine chemical equilibria under the impact of mechanical forces. Corresponding studies of this type are reviewed in the last section.

Contents

Fig. 1 Snapshots of a polymer coil, generated by Monte Carlo simulation of the bond fluctuation model on the simple cubic lattice with a square well attraction of range $\lambda = \sqrt{6}$ lattice spacings. For temperature $T \rightarrow \infty$ the effective monomers (which block all eight sites of an elementary cube of the lattice from further occupation) interact with excluded volume forces and one has very good solvent conditions, Both the mean square end-to-end distance $\langle R_e^2 \rangle$ and the mean square gyration radius $\langle R_g^2 \rangle$ then scale with the number of effective monomers along the chain (henceforth denoted as "chain length" N) as $N^{2\nu}$, with $\nu \approx 0.588$ (*left*). When the temperature is finite, one reaches the θ-temperature (*middle*) where the attractive interactions effectively "cancel" the repulsions, $\nu = 1/2$ (*middle*). For $T \ll \theta$ (*right*), the chain takes a compact configuration, $\nu = 1/3$. This compact configuration may either be a (fluid) globule or a (solid) crystal or an amorphous solid (glass). The snapshots all refer to $N = 64$. Adapted from Binder et al. [4]

1 Phase Behavior, Structure, and Elastic Properties of Single Chains

1.1 Phase Behavior of Coarse-Grained Single-Chain Models

Manipulation of single polymer chains has become a major direction of research in polymer science because such experiments can yield valuable insight into the relationship between the chemical structure and physical properties of macromolecules [1–3]. Such experiments do also depend on the conditions of the environment of the polymers, e.g., in an experiment where colloidal beads attached to the chain ends of a biopolymer are moved away from each other with laser tweezers. Then, the extension $\langle X \rangle$ versus force (f) relation will depend on the quality of the solvent in which the polymer has been dissolved. Also, the structure of a polymer adsorbed on a substrate from solution will depend on the solvent quality [4, 5].

When one addresses such questions via computer simulation of suitable models, knowledge of the phase behavior of the macromolecule in bulk solution (and how this is controlled by various parameters) is a necessary ingredient of the modeling study [4–14]. Figure 1 reminds the reader about the classic textbook view of this problem, with swollen coils (Fig. 1, left) under good solvent conditions, essentially Gaussian coils (Fig. 1, middle) under Theta solvent conditions, and collapsed dense globules in poor solvents (Fig. 1, right) [15]. However, this is not the whole story:
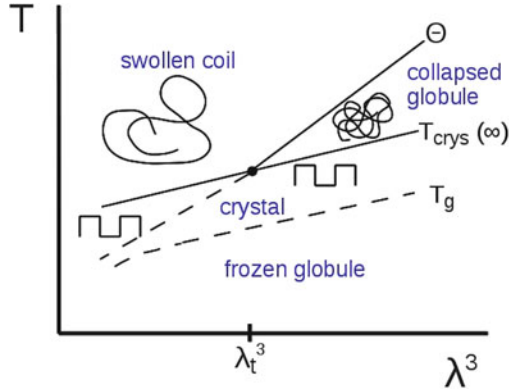
Fig. 2 Schematic phase diagram of a single flexible polymer chain in the thermodynamic limit ($N \to \infty$) as a function of temperature T and range of attractive monomer–monomer interaction λ. For $\lambda > \lambda_t$, there occurs a transition at $T = \theta(\lambda)$ from the swollen coil to the collapsed fluid globule. At $T_{\mathrm{cryst}}(N = \infty)$ the globule crystallizes. Due to slow crystallization kinetics, this transition may be undercooled and at $T_g < T_{\mathrm{cryst}}(\lambda)$ the collapsed globule freezes into a glassy state. Since it was assumed that the transition lines vary linearly with the interaction volume λ^3, λ^3 rather than λ has been chosen as an abscissa variable. Adapted from Binder et al. [4]

although properties such as the asymptotic exponent (ν) describe how the size of the polymer scales with its chain length (N) and do not depend on details of the monomer–monomer interaction, this is not true for the structure of the compact state. Both the bond fluctuation model [4–11] and a simple off-lattice model (tangent hard spheres with a square well attraction of range λ, in units of the sphere diameter σ) [12–14] exhibit a phase diagram of the type shown in Fig. 2 [4]. Only for $\lambda \geq \lambda_t$, does one encounter the classic picture [15] of Fig. 1. For $\lambda < \lambda_t$, one does find a direct (first-order-like) transition from the swollen coil to the crystal; no θ-like behavior can occur in thermal equilibrium. Thus, for $\lambda = \lambda_t$ one encounters (in thermal equilibrium) a triple point, where swollen coils, collapsed fluid globules, and crystallized states of the polymer coexist. Sharp transitions of single chains can occur in the thermodynamic limit $N \to \infty$ only; for chains of finite chain lengths N, the transition is rounded (and shifted) [6–11]. By "rounding" of a transition due to finite size N one means that the singularity that appears for $N \to \infty$ (e.g., the divergence of the specific heat) is smeared out over some temperature region. The width of this region shrinks to zero as $N \to \infty$. But, one can provide theoretical arguments (and verify them by simulations) [6–10] that the extent of rounding and shifting scales like $N^{-1/2}$ for the coil–globule transition. For the coil–crystal transition, the shift scales like $N^{-1/3}$ and for the rounding like N^{-1}, so it is comparatively much sharper [12, 13]. In the simulations, the transitions are conveniently studied in the microcanonical (constant energy E) ensemble rather than the conjugate canonical (constant temperature T) ensemble [11, 14].

The models discussed so far assume that the macromolecules are fully flexible down to the smallest scales that are considered. This assumption is often not a good

approximation. If one includes local chain stiffness in the model, the swollen state and the Theta state in Fig. 1 still persist, whereas the compact states are modified. Bond vectors between neighboring monomers along the chain try to develop some local nematic-type order, but the chain connectivity constraint and the tendency to form compact structures are then in some conflict, which can, e.g., be resolved by the formation of toroidal structures [4, 16]. However, an exhaustive study of the phase diagram of a single chain as a function of stiffness, strength, and range of attractive effective monomer–monomer interactions, and chain length is still a task for the future.

1.2 Force Versus Extension Behavior in the Good Solvent Regime

In this subsection, we focus on long chains under good solvent conditions, where a rather universal behavior of the polymers (irrespective of the details of the model that is studied) [15] can be expected. Hence, we focus on the simplistic self-avoiding walk (SAW) model on the simple cubic lattice, but we include the effect of chain stiffness (introducing an energy penalty ϵ_b whenever the SAW makes a 90° kink). This extension of the model is crucial when one has in mind the application to biopolymers (such as double-stranded DNA, which has a persistence length $\ell_p = 50$ nm but a chain diameter of only $D = 3$ nm) [1, 2]. This model can be studied very efficiently with the PERM algorithm (pruned-enriched Rosenbluth method) [17, 18], which allows the study of rather long chains (e.g., up to $N = 50,000$). This algorithm directly estimates the partition function of the chain (and hence its free energy) as a function of N, $q_B = \exp(-\epsilon_b/k_BT)$ and the Boltzmann factor due to the force [$\exp(f\ell_b/k_BT)$, where the bond length ℓ_b is simply the lattice spacing, taken as unit of length]. This model hence allows contact with the Kratky–Porod [19] worm-like chain (WLC) model, which is used as a standard model of semiflexible macromolecules [1, 2]. However, the Kratky–Porod model neglects excluded volume completely and hence necessarily fails (under good solvent conditions) for long chains.

Figure 3a shows a plot of $3\left\langle R_g^2 \right\rangle/\ell_p L$, where $L = N\ell_b = N$ is the contour length of the semiflexible chain, versus $n_p = L/\ell_p$, the contour length in units of the persistence length, for zero stretching force, $f = 0$ [20]. This representation is chosen such that the Kratky–Porod result reduces to a master curve, which saturates at unity for large n_p. It is seen that for $n_p \leq 1$ all data coincide on a straight line, described by $\left\langle R_g^2 \right\rangle = L^2/12$ (or $3\left\langle R_g^2 \right\rangle/(\ell_p L) = 0.25(L/\ell_p)$, respectively). This is the trivial result for rigid rods. For $1 < n_p < 10$, a gradual crossover towards the behavior of SAWs occurs, $\left\langle R_g^2 \right\rangle/L \propto L^{2\nu - 1}$, if the chains are rather flexible. If the chains are rather stiff, an intermediate Gaussian regime sneaks in (in $d = 3$ dimensions only), before a second crossover to SAW-like behavior
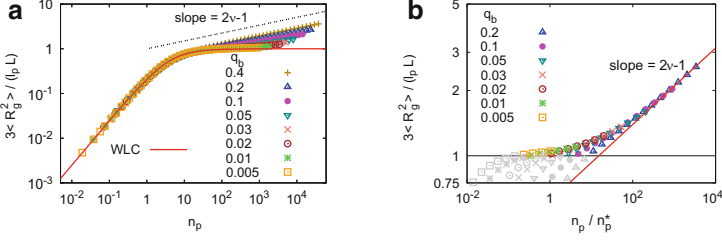
Fig. 3 Log–log plot of the normalized mean square gyration radius $3\langle R_g^2\rangle/(\ell_p L)$ versus $n_p = L/\ell_p$ (**a**) or versus n_p/n_p^* (**b**) where n_p^* has been chosen such that the data for large n_p coincide on the straight line with slope $2v-1$, as indicated. Both parts include data for widely varying chain stiffness (note that $\ell_p \approx q_b^{-1}/4$ for small q_b in $d = 3$ dimensions). (**a**) The Kratky–Porod model for all L, ℓ_p yields a unique master curve, denoted *WLC*. The horizontal part of this curve is also included in (**b**). Reprinted with permission from [20]. Copyright 2012, American Institute of Physics

occurs (at $n_p = n_p^*$, see Fig. 3b). Flory theory [21, 22] predicts that $n_p^* \propto (\ell_p/D)^2$ whereas the simulations seem to suggest that $n_p^* \propto (\ell_p/D)^{2.5}$ [22]. It is also important to note that in $d = 2$ dimensions, a case relevant for polymers strongly adsorbed on planar substrates, no such intermediate Gaussian behavior occurs; instead, one crosses over from rigid rods to $d = 2$ SAWs, with $\langle R_g^2\rangle \propto \ell_p^{1/2}L^{3/2}$, irrespective of how large ℓ_p is, as soon as $n_p > 1$ [22]. The simulation results in Fig. 3 imply two successive crossovers, from rods to Gaussian random walks and from these simple random walks to swollen coils exhibiting SAW statistics, and are in very good agreement with experiments on semiflexible synthetic polymers [23]. For double-stranded DNA, however, the estimate $l_p \approx 50$ nm implies that excluded volume effects become important only if L exceeds 100 nm. These deviations from the Kratky–Porod model also invalidate its predictions for the force versus extension curve [1, 2]:

$$\langle X\rangle/L \propto f\ell_p/k_B T \ (\text{small } f), \ \ 1 - \text{const}(f\ell_p/k_B T)^{-(1/2)} \ (\text{large } f) \ . \quad (1)$$

In $d = 3$ dimensions, a useful interpolation formula between both regimes is:

$$\frac{f\ell_p}{k_B T} = \left[\frac{1}{4}\left(1 - \frac{\langle X\rangle}{L}\right)^{-2} + \frac{\langle X\rangle}{L} - \frac{1}{4}\right], \quad (2)$$

which will be used in later sections of this chapter for simplicity. So, irrespective of dimensionality, there is a wide regime of linear response and then the extension of the chain along the direction of the force ($\langle X\rangle$) simply saturates at the contour length. However, in reality the regime of linear response is very restricted: One has $\langle X\rangle/L \propto (\langle R_e^2\rangle/L)f/k_B T$ until for $f/k_B T \propto 1/\sqrt{\langle R_e^2\rangle}$ a crossover to

a

b
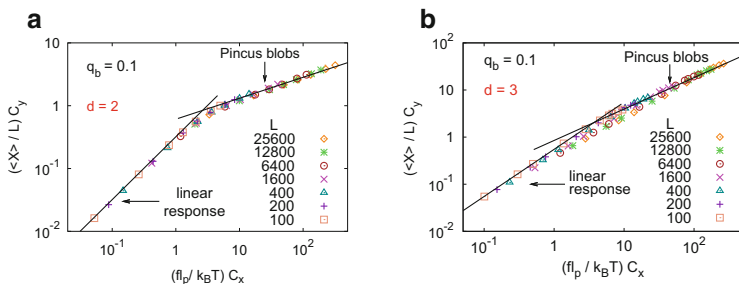
Fig. 4 Log–log plot of scaled extension versus force curve, $(\langle X \rangle /L)C_y$ versus $(f\ell_p/k_BT)C_x$, for moderately stiff chains ($q_b = 0.1$), both in $d = 2$ (**a**) and in $d = 3$ (**b**). Contour lengths from $L = 100$ up to $L = 25{,}600$ are included. The two *straight lines* have the theoretical slopes appropriate for the linear response (for small f) and for the nonlinear Pincus regime, respectively. (**a**) The scaling factors $C_x = (L/\ell_p)^{3/4}$ and $C_y = (L/\ell_p)^{1/4}$ are used according to our theory [20]; estimates for ℓ_p were obtained independently from the initial decay of the bond vector autocorrelation function $\left\langle \vec{a}_i \cdot \vec{a}_{i+s} \right\rangle$ as function of the index s along the chain. (**b**) In $d = 3$, the predicted scaling factors $C_x = \left(L^3 \ell_b / \ell_p^4\right)^{1/5}$, $C_y = \left[L^2/(\ell_b \ell_p)\right]^{1/5}$ were used. Reprinted with permission from [22]. Copyright 2012, American Institute of Physics

a nonlinear regime (first proposed by Pincus [24]) occurs, where $\langle X \rangle /L \propto \left(f\ell_p/k_BT\right)^{2/3}$ $\left(\ell_p/R^*\right)^{1/3}$ with $R^* \propto \ell_p^2/D$ (in $d = 3$). However, this Pincus regime is only observable for $n_p > n_p^*$. In $d = 2$ dimensions, the nonlinear Pincus regime is described simply by $\langle X \rangle /L \propto \left(f\ell_p/k_BT\right)^{1/3}$, and this regime extends until saturation of $\langle X \rangle$ at L starts. So, in $d = 2$, the Kratky–Porod model also fails completely with respect to the force–extension behavior, whereas in $d = 3$ it holds for very stiff and thin chains (for which $n_p^* \gg 1$), if they are not too long ($n_p < n_p^*$).

The various crossover predictions and the numerical evidence that we have obtained for these crossovers are described in detail in two long papers [20, 22]; here we show only two examples that illustrate the crossover from the linear response to the Pincus regimes, both in $d = 2$ and $d = 3$ dimensions (Fig. 4). We stress that the widely used interpolation formula for the force versus extension curve quoted in Eq. (2) does not include the Pincus regime.

We emphasize that these deviations from the Kratky–Porod model that occur for semiflexible polymers both in equilibrium and in their response to stretching forces, were not properly noticed in most of the experiments. However, in analyzing data one normally does not have strictly monodisperse chains, and neither ℓ_p nor L are independently known; both parameters are usually used as adjustable fitting parameters. Because ℓ_p depends on d, and is also affected by solvent conditions, and for strongly stretched real chains other effects (related to the local chemical structure of the effective monomeric units) come into play, this failure is not surprising. However, some of the confusion over the actual values of ℓ_p that

can be found in the literature for specific polymers can be attributed to such problems. But, it is reassuring that in a few recent experiments evidence for several crossovers in $\langle X \rangle$ versus f curves and for the nonlinear Pincus behavior have been found [25].

The problem of understanding the persistence length and its consequences is also taken up by Butt et al. [26]: for bottle-brush polymers, there is the challenging problem of understanding how their stiffness depends on the grafting density and degree of polymerization of the grafted side chains.

## 1.3 Single Chain Collapse Versus Adsorption

The studies on single-chain adsorption on flat substrates were based on the same models used for the studies of single chains in the bulk, as described above. One issue that was addressed is the competition between adsorption, collapse, and crystallization of tethered single chains [5].

Figure 5 presents a tentative "diagram of states" for $N = 64$ (we should speak about "phase diagrams" only in the limit $N \rightarrow \infty$, so the lines in the diagram of states are not sharp phase boundaries, but rather various signatures of smooth crossovers). Here, we use $\beta_b = \epsilon/k_BT$ and $\beta_s = \epsilon_s/k_BT$ as control parameters (ϵ and ϵ_s denote the strength of the attractive energy between monomers and between monomers and the substrate surface, respectively). Due to the competition between the structures identified in the bulk (Fig. 2) and various quasi-two-dimensional wall-attached structures, the phase diagram emerging in the limit $N \rightarrow \infty$ for the bond fluctuation model of a polymer interacting with the surface (and allowing for variable solvent conditions) is still incompletely understood [5].

When we restrict attention only to the good solvent case, the PERM [17, 18] algorithm applied to the simple SAW model on the simple cubic lattice can be used again, and very long chains can be simulated (see Sect. 1.2). Although adsorption of single flexible polymers under good solvent conditions is a classical problem that has been studied for decades [27–32], very important aspects are still controversial. One such aspect is the value of the crossover exponent ϕ, which controls the number of adsorbed monomeric units N_s right at the adsorption threshold. Although $\phi = 1/2$ for Gaussian chains is well known, de Gennes [33] suggested a scaling relation $\phi = 1 - \nu$, which would imply $\phi \approx 0.41$. However, then it was shown that this scaling relation should hold only for a chain tethered to a freely penetrable interface, but not to an impenetrable surface [27, 28]. Early simulations [27] gave $\phi \approx 0.59$, but later investigations came up with different values; the smallest estimate so far is Grassberger's [30] estimate of $\phi \approx 0.48$, but there has not yet been any consensus on a value of this exponent. Bhattacharya et al. [31] observed that, depending on the degree of interaction between different loops, one could get any value in the range $0.39 \le \phi \le 0.59$. Should one draw then the conclusion that this exponent is nonuniversal?

To test this question, the SAW tethered to an impenetrable wall has been studied, using a square well adsorption potential of depth U and range W. If universality
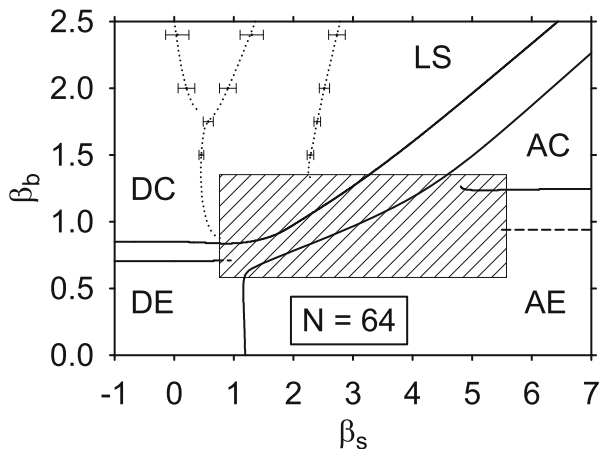
Fig. 5 Diagram of states for a tethered chain, described by the bond fluctuation model on the simple cubic lattice, for chain length $N = 64$, in the plane of variables bulk coupling β_b and surface coupling β_s. The *solid lines* show the location of well-defined maxima in the fluctuation of surface contacts or bead–bead contacts, respectively; *broken* and *dotted lines* show the locations of less well-pronounced anomalies in these fluctuations. In the *hatched region*, the precise behavior is still uncertain. The states that compete with each other are desorbed expanded (*DE*, i.e., a three-dimensional mushroom); adsorbed expanded (*AE*, i.e., a $d = 2$ SAW), desorbed collapsed (*DC*, as in Fig. 1b, but tethered to the grafting plane); adsorbed collapsed (*AC*, a compact but disordered structure with many surface contacts); and various crystalline layered structures (*LS*). Reprinted with permission from [5]. Copyright 2008, American Institute of Physics
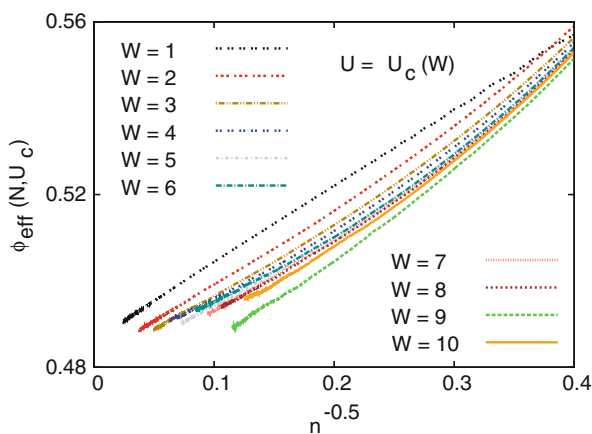
Fig. 6 Plot of the effective crossover exponent $\phi_{\mathrm{eff}}(N)$ versus $n^{-0.5}$ at $U = U_c(W)$ for the different choices of W, as indicated. Note that $\phi_{\mathrm{eff}}(N,U,W)$ is defined as $\phi_{\mathrm{eff}}(N,U,W) = \ln\left\{ \frac{4\theta_s(2N,U,W)}{\theta_s(N/2,U,W)} / \ln 4 \right\}$, where θ_s is the fraction of adsorbed monomers at the surface. Reprinted with permission from [32]

holds, the location $U_c(W)$ of the transition will depend on W, but not the critical exponents. Klushin et al. [32] showed that indeed all exponents are independent of the parameter W, but for the crossover exponent there occurs a correction term ($\propto N^{-1/2}$), whose amplitude (which is not expected to be universal) strongly depends on W. However, if we introduce a blob picture such that $N = ng$, where g is the number of monomers per blob, n is the number of blobs, and the blob diameter (g^ν) is chosen equal to W, one finds that all systems behave rather similarly (Fig. 6) [32]. It also is evident that for smaller values of N the effective crossover exponent is distinctly larger than 0.5, whereas for $N \to \infty$ the Grassberger [30] estimate $\phi \approx 0.48$ is confirmed. The conclusion that ϕ is universal is also confirmed by a study of the loop length distribution function at $U = U_c(W)$, which is found to satisfy a universal power law (in the limit $N \to \infty$).

Another interesting question is the effect of chain stiffness on polymer adsorption. It has been found [34] that increase of $\ell_p \to \infty$ causes a crossover in the character of the adsorption transition from second order (for finite ℓ_p) to first order as ℓ_p diverges. This finding is compatible with mean field theories [35]. However, a complication that has not been analyzed before is the finding that the persistence length ℓ_p is not only dependent on the bending potential, but also depends on the distance from the adsorption transition [34].

1.4 Adsorption of Single Chains

1.4.1 Copolymer Localization on Selective Liquid–Liquid Interfaces

The behavior of hydrophobic–polar (amphiphilic) copolymers (HP-copolymers) at a selective interface (the interface that divides two immiscible liquids, say, water and oil, each liquid being a good solvent for one type of monomer and bad for the other) is of great importance in the chemical physics of polymers. HP-copolymers are readily localized at such an interface because, under a sufficiently large degree of selectivity, the hydrophobic (H) and polar (P, hydrophilic) parts of a copolymer chain try to stay on different sides of the interface due to the interplay between the entropy loss in the vicinity of the interface and the energy gain in the proper solvent (cf. Fig. 7). Not surprisingly, during the last two decades the problem has attracted a lot of attention and has been looked at experimentally [37–39], theoretically [40, 41], and in computer experiments [42]. In earlier studies, attention was mostly focused on diblock copolymers [37, 38] due to their relatively simple structure, but the scientific interest shifted later to random HP-copolymers at penetrable interfaces [41, 43, 44]. In contrast, our investigations have focused mainly on unexplored aspects such as the impact of block size M on the static properties and on the localization kinetics of regular multiblock copolymers at the phase boundary between the two immiscible solvents. We showed that these are well described by a simple scaling theory [36, 45, 46] in terms of the total copolymer length
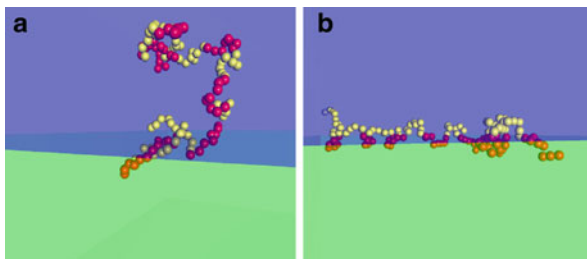
Fig. 7 Snapshots of typical configurations of a copolymer with chain length $N = 128$ and block length $M = 8$ on the verge of adsorption threshold at $\chi = 0.25$ (**a**) and in the strong localization limit $\chi = 10$ (**b**). The value of the critical selectivity of this chain is $\chi_c = 0.67$. Reprinted with permission from [36]. Copyright 2005, American Institute of Physics

N (the number of repeating units in the chain) and the block size M (the number of consecutive monomers of the same kind) as well as the selectivity parameter χ, that is, the energy gained by a monomer when in the more favorable solvent.

Our scaling description is based on the idea that a multiblock copolymer can be treated as a "coarsened" homopolymer where a single HP-diblock plays the role of an effective segment. All such diblocks try to keep their H- and P-segments in the corresponding preferred environment. This leads to the diblock "polarization" at the interface and to a free energy gain, which produces an effective attraction energy E. This means that the energy gain χ (i.e., the selectivity parameter) for a P-monomer in its own (polar) environment is equal to the corresponding energy gain for a H-monomer, provided the latter stays in the hydrophobic environment. An estimate for the effective attraction energy per diblock of length $2M$ in the symmetric case yields $E \propto - \chi^2 M^2$ [47], where the energy is measured in units of k_BT, k_B denoting the Boltzmann constant. In terms of the selectivity parameter, there are three adsorption regimes that can be distinguished:

For χ smaller than a critical value χ_c, the interface is too weak to affect the polymer so that the macromolecule conformation is identical to that in the absence of an interface

For $\chi \simeq \chi_c$, the copolymer is captured by the interface yet is not strongly deformed (weak localization)

For $\chi \simeq \chi_\infty > \chi_c$, the interface is strong enough to induce a perfect flattening of the copolymer so that all the monomers are in their preferred environment (strong localization) (cf. Fig. 7b)

Various quantities, such as the fraction of repeating units (monomers) captured at the interface (which serves as an order parameter of the localization phase transition) and the components of the polymer radius of gyration parallel ($R_{g\parallel}$) and perpendicular ($R_{g\perp}$) to the phase boundary between the immiscible liquids, can be then studied in order to verify the predictions of the pertinent scaling analysis by comparison with results from Monte Carlo simulations [36, 45–47]. As an example, we show the changing degree of copolymer localization (Fig. 8a) and the ensuing
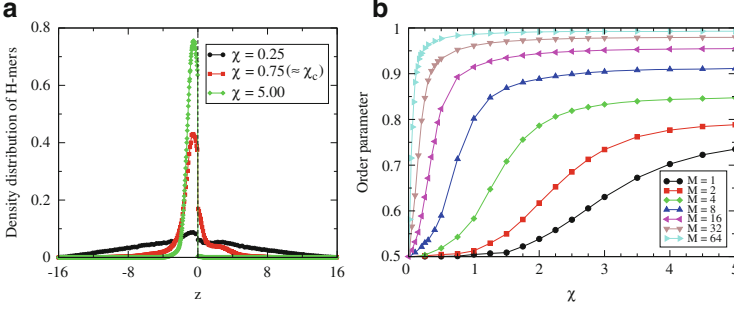
Fig. 8 (**a**) Density distribution of hydrophobic monomers (*H-mers*) for a chain with $N = 128$ and $M = 8$ at different χ. Here $\chi_c = 0.67$. (**b**) Fraction of polar and hydrophobic monomers (order parameter) in the polar (at $z > 0$) and hydrophobic (at $z < 0$) semispace versus selectivity χ for $N = 128$ and different block sizes M. Reprinted with permission from [36]. Copyright 2005, American Institute of Physics

interface thickness as the selectivity χ is varied (Fig. 8b). In fact, the copolymer localization at selective interface can be considered as a sharp phase transition in the limit $N \to \infty$, $M \to \infty$, and $\chi \to 0$. As an appropriate variable η in the various scaling relations one may use the number of blobs, $\eta \equiv \chi N^{(1 - \nu)/2} M^{(1 + \nu)/2}$ (here $\nu \approx 3/5$ denotes the Flory exponent). At finite χ, chain length (N), and block length (M), the transition looks like a smooth crossover, described by an order parameter in terms of the fraction of P- and H-monomers on both sides of the penetrable interface, (cf. Fig. 8b). Generally, in a very good agreement between theoretical predictions and our simulation data, one may conclude that the scaling theory correctly captures the most salient features related to the copolymer behavior at penetrable boundaries between selective solvents:

- The critical selectivity decreases with growing block length as $\chi_c \propto M^{-(1 + \nu)/2}$, while the crossover selectivity to the strong localization regime obeys a simple relation $\chi_\infty \propto 1/M$
- The size of the copolymer varies in the weak localization regime as $R_{g\perp} \propto M^{-\nu(1 + \nu)/(1 - \nu)}$ and $R_{g\parallel} \propto M^{[(\nu_2 - \nu)(1+\nu)]/(1-\nu)}$, where $\nu_2 = 3/4$ is the Flory exponent in 2D space
- In the regime of strong localization, one obtains $R_{g\perp} \propto M^\nu$ and $R_{g\parallel} \propto M^{-(\nu_2 - \nu)} N^{\nu_2}$, respectively

For the most relevant case of strong localization, the kinetics of copolymer adsorption is of particular importance. A simple analytical theory based on scaling considerations has been proposed and shown to provide a faithful description for the relaxation of the initial copolymer coil into a flat-shaped layer [45]. This conformational change of a chain for $\chi > \chi_\infty$ can be considered to be governed by an attractive force, $f_{attr}^\perp \approx - \chi_\infty N/R_{g\perp}$, and an opposing force of confinement, $f_{conf} \approx Na^{1/\nu}/R_{g\perp}^{1/\nu + 1}$, which yield a set of dynamic equations:
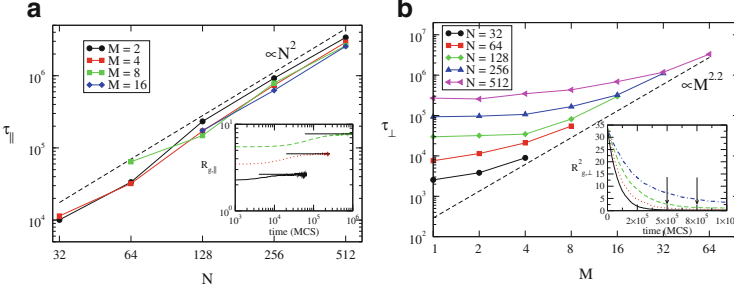
Fig. 9 (**a**) Variation of $\tau_\parallel$ with N for blocks of size $M = 2, 4, 8,$ and 16. The *inset* shows typical behavior of $R_\parallel(t)$. (**b**) $\tau_\perp$ versus block length M for chains with $32 \leq N \leq 512$. *Dashed line* denotes the predicted slope of ≈ 2.2. The *inset* shows typical relaxation of $R_{g\perp}^2(t)$ for $N = 256$, $M = 2$. Reproduced by permission from [45]. Copyright 2006, IOP Publishing

$$\zeta_0 N \frac{dR_{g\perp}}{dt} = -\frac{\chi_\infty N}{R_{g\perp}} + \frac{Na^{1/\nu}}{R_{g\perp}^{1/\nu+1}}, \quad \zeta_0 N \frac{dR_{g\parallel}}{dt} = \frac{\nu N^2}{R_{g\parallel}^3 R_{g\perp}} - \frac{R_{g\parallel}}{aN} \tag{3}$$

where the second equation in Eq. (3) describes the horizontal (or parallel to the interface) spreading due to steric repulsion (excluded volume effects), and ζ_0 denotes the monomer friction. One may find solutions for the set of equations of motion (3) and determine the characteristic times for relaxation perpendicular ($\tau_\perp$) and parallel ($\tau_\parallel$) to the interface (cf. Fig. 9). The observed agreement with simulation data is very good, and an important distinction between early and late stages of localization can be demonstrated. A careful analysis in terms of localization-induced coupling of (otherwise independent) Rouse modes reveals [47] a strong coupling of the first few modes as a consequence of the interplay between the interface and the regular block structure of the polymer. Summarizing, one may conclude that:

- The typical time for lateral diffusion in the case of strong localization varies as $\tau \propto M^{2(\nu-\nu_2)}N^{2\nu_2+1}$ [36]
- The characteristic times for localization perpendicular and parallel to the interface at strong selectivity scale as $\tau_\perp \propto M^{1+2\nu}$ and $\tau_\parallel \propto N^2$, respectively [45]
- The averaged components of the Rouse modes of a copolymer, adsorbed at a liquid–liquid interface, are not mutually orthogonal as in the bulk but significantly coupled for small indices p, with the coupling gradually vanishing as the mode number p grows [46]

Our studies have revealed that a selective liquid–liquid interface can be very sensitive with respect to the composition (most notably, the block size M) and chain length N of a multiblock copolymer chain. This sensitivity suggests an interesting possibility to use selective liquid–liquid interfaces as a new type of chromatography, whereby one can "sieve" (i.e., separate and analyze) complex
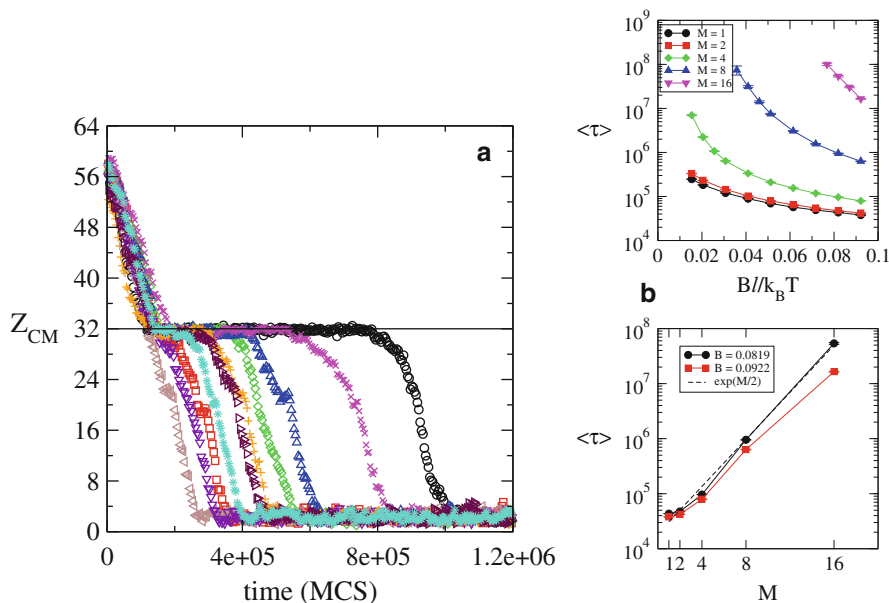
Fig. 10 (**a**) Time transients of the chain center of mass motion $Z_{CM}(t)$ during the drift of a copolymer with $N = 256$ and $M = 4$ at field intensity $B = 0.031$ for 10 individual runs, indicating different capture times during crossing of the interface. The interface position is at $Z = 32$. Reprinted with permission from [47]. Copyright 2006 Wiley Periodicals, Inc. (**b**) Variation of the mean capture time $\langle \tau \rangle$ with field strength B for copolymers of length $N = 128$ and different block size M. *Dashed line* denotes an exponential fit. Reprinted with permission from [48]. Copyright 2006 American Chemical Society

mixtures of copolymers with respect to block size and chain length. Thus, a chain may be driven from an initial configuration, some distance away from the interface, into the other half of the container whereby it will pass through the penetrable interface. Depending on their length and composition, different chains will then be temporarily trapped at the plane separating the two solvents. One might expect that the characteristic "capture" time would strongly depend on the particular properties of the chain, so that for a given field intensity B some chains would stick for a long time at the interface, whereas others with different M and N will pass rapidly through it (cf. Fig. 10). This possibility has been considered both theoretically and by means of computer experiment in our investigations [47, 48], and the scaling of the typical "capture" times τ with copolymer and block length N and M elucidated. For chains driven by an external field through a selective interface, one finds that the mean capture time τ displays a non-Arrhenian dependence on the field intensity B, and increases almost exponentially with the block size M (cf. Fig. 10).

Finally, it is worth mentioning that in the rich behavior of copolymers at selective liquid–liquid interfaces we have not included results pertaining to random copolymers, where the range of sequence correlations plays a role similar to that

of the block size. Moreover, in our considerations we have largely ignored the possible effects of hydrodynamic interactions, even though the case of Zimm dynamics was accounted for in our scaling approach [47]. Also, the penetrable interface has been considered in the simplest approximation of zero thickness although the existence of some intrinsic width, capillary waves, etc. might add additional facets to the overall picture. Thus, a variety of details are relegated to further studies and the reported results should be seen as a first step into a fascinating field of phenomena that might offer a broad perspective for application and development.

1.4.2 Single Chain Adsorption: Statics and Kinetics

Adsorption of polymers on surfaces plays a key role in numerous technological applications and is also relevant to many biological processes. During the last three decades it has been constantly a focus of research interest. The theoretical studies of the behavior of polymers interacting with solid substrate have been based predominantly on both scaling analysis [49] as well as on the self-consistent field (SCF) approach [50]. The close relationship between theory and computer experiments in this field [27, 51] has proved especially fruitful. Most investigations focus on the determination of the critical adsorption point (CAP) location and on the scaling behavior of a variety of quantities below, above, and at the CAP.

The investigations mentioned above have been devoted exclusively to homopolymers, but the adsorption of copolymers (e.g., multiblocks or random copolymers) is still much less understood. Thus, for instance, the CAP dependence on block size M at fixed concentration of the sticking A-mers is still unknown, as are the scaling properties of regular AB-multiblock copolymers in the vicinity of the CAP. The main focus of our investigations [52] has been aimed at the adsorption transition of random and regular multiblock AB-copolymers on a rigid substrate. We have used two different models to establish an unambiguous picture of the adsorption transition and to test scaling predictions at criticality. The first model is an off-lattice coarse-grained bead-spring model of polymer chains that interact with a structureless surface by means of a contact potential, once an A-monomer comes close enough to be captured by the adsorption potential. The second model is the pruned-enriched Rosenbluth method (PERM) on a cubic lattice, which is very efficient, especially for very long polymer chains, and provides high accuracy of the simulation results at criticality. Notwithstanding their basic difference, both methods suggest a consistent picture of the adsorption of copolymers on a rigid substrate and confirm the theoretical predictions, even though the particular numeric values of the CAP are model-specific and differ considerably.

As one of the central results of our studies, one should point out the phase diagram of regular multiblock adsorption, which gives the increase in the critical adsorption potential $\epsilon_c(M)$ with decreasing length M of the adsorbing blocks (cf. Fig. 11a). For very large block length, $M^{-1} \to 0$, we find that the CAP systematically approaches that of a homogeneous polymer. We demonstrate also
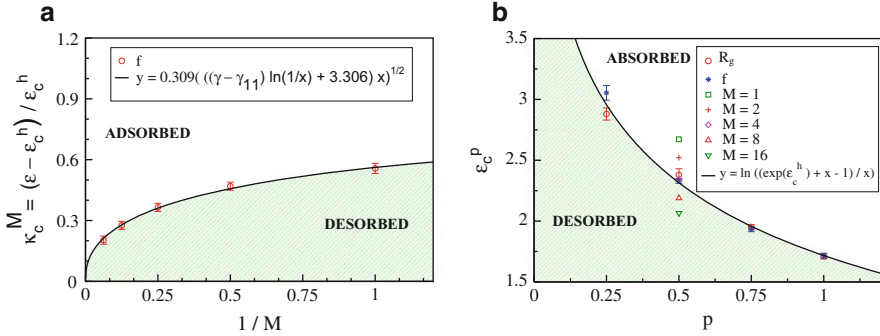
Fig. 11 (**a**) Phase diagram showing the variation in critical adsorption strength $\kappa_c^M = (\epsilon_c^M/\epsilon_c^h) - 1$ with block length M. (**b**) Critical adsorption potential (CAP) versus composition p for random copolymers. *Solid line* is a best fit of the theoretical prediction $\epsilon_c^p = ln[(exp\epsilon_c^h + p - 1)/p]$. Here, CAP $\epsilon_c^h = 1.716$. *Symbols* denote the CAP for multiblock copolymers with block size M. Reprinted (adapted) with permission from [52]. Copyright 2008 American Chemical Society

that the phase diagram, derived from computer experiment, agrees well with the theoretical prediction based on scaling considerations.

The phase diagram for random copolymers with quenched disorder that gives the change in the critical adsorption potential, ϵ_c^p, with changing percentage of the sticking A-monomers, p, has also been determined from extensive computer simulations carried out with the two employed models (cf. Fig. 11b). We observed perfect agreement with the theoretically predicted result, $\epsilon_c^p = \ln\left[\frac{\exp(\epsilon_c^h)+p-1}{p}\right] \geq \epsilon_c^h$ (where ϵ_c^h is the critical attraction energy of an effective homopolymer [53]), which has been derived by treating the adsorption transition in terms of the "annealed disorder" approximation. We show that a consistent picture appears of how some basic polymer chain properties of interest, such as the gyration radius components perpendicular and parallel to the substrate or the fraction of adsorbed monomers at criticality, scale when a chain undergoes an adsorption transition regardless of the particular simulation approach. An important conclusion thereby concerns the value of the universal crossover exponent $\phi \approx 0.5$, which is found to remain unchanged regardless of whether homopolymers, regular multiblock polymers, or random polymers are concerned.

The adsorption kinetics of a single polymer chain on a flat structureless plane has been examined in the strong physisorption regime [53]. Adopting the stem-flower model for a chain conformation during adsorption, and assuming the segment attachment process to follow a "zipping" mechanism, we developed a scaling theory that describes the time evolution of the fraction of adsorbed monomers for polymer chains of arbitrary length N at adsorption strength of the surface ϵ/k_BT. To this end, we derived a master equation as well as the corresponding Fokker–Planck equation for the time-dependent probability distribution function (PDF) of the number of adsorbed monomers and for the complementary PDF of chain tails. Inherent in this derivation is the assumed condition of detailed balance, which makes it possible
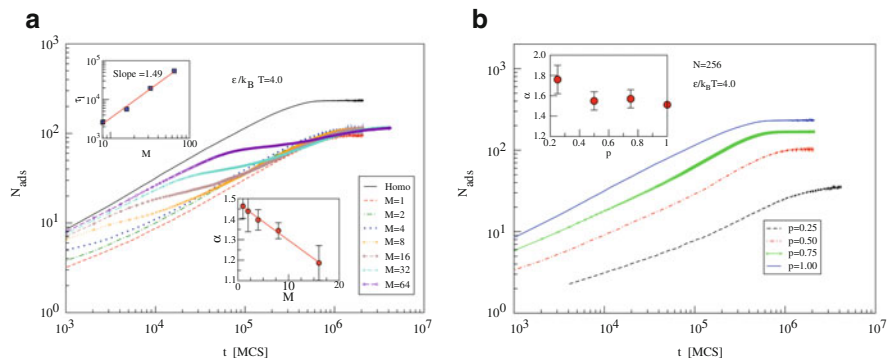
Fig. 12 (**a**) Number of adsorbed segments $N_{ads}(t)$ versus time t for regular AB copolymers with length $N = 256$ and different block size M. The time interval of the transient "shoulders" is shown in the *upper inset*. The *lower inset* displays the variation in the scaling exponent α for the time of adsorption $\tau \propto N^\alpha$ with block length M. (**b**) The same plot for a random copolymer with $N = 256$ and different composition p; $p = 1$ corresponds to the case of a homopolymer. The variation of α with p is shown in the *inset*. Reprinted with permission from [53]

to relate the elementary steps of adsorption and desorption. From the numeric solution of the equivalent discrete set of coupled first-order differential equations, we find that the growth of the adsorbed fraction of monomers with time is governed by a power law, $n(t) \propto t^{[1/(1 + \nu)]}$, while the typical time of adsorption τ scales with the length of the polymer N as $\tau \propto N^\alpha$, with $\alpha = 1 + \nu$. In Fig. 12 we display the variation in the number of adsorbed segments N_{ads} with time t for regular copolymers with block size M and for random copolymers with percentage p of the "sticking" segments. The adsorption transients found in the Monte Carlo simulation are in good agreement with these predictions, if one takes into account the finite-size effects due to the finite length of the studied polymer chains. One could also conclude that, in the case of regular multiblock and random copolymers, the adsorption kinetics strongly resembles that of homopolymers.

It should be also mentioned that a lot of insight and information regarding the adsorption of single chains on a solid substrate can be gained from the PDFs of the various building units, trains, loops, and tails that an adsorbed chain is formed of. In the literature [53] one may verify that the theoretically derived and predicted exponential expression for the PDF of trains appears to comply very well with simulation data.

1.5 Manipulation of Single Chains: Force-Induced Detachment and Translocation Through Pores

1.5.1 Detachment of Adsorbed Polymer Chain: Statics and Dynamics

With the development of novel single macromolecule experiments, the manipulation of individual polymer chains and biological macromolecules is becoming an important method for understanding their mechanical properties and characterizing
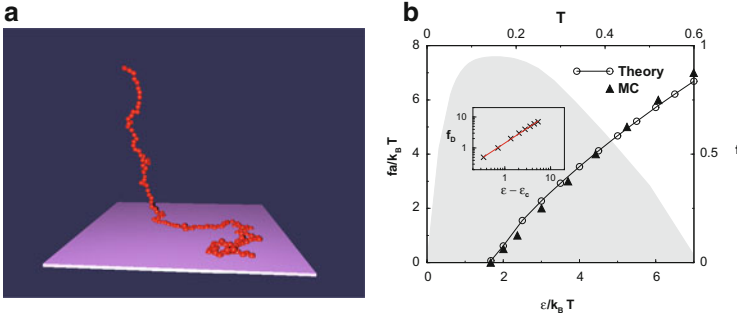
Fig. 13 (**a**) Snapshot of an adsorbed polymer chain with length $N = 128$, partially detached from the plane by external force $f_M = 6.13$ that keeps the end monomer at height $h = 25\sigma$. Reprinted with permission from [31]. Copyright 2009, American Chemical Society. (**b**) Critical detachment force $f_D = f\sigma/k_BT$ versus surface potential ϵ/k_BT. *Triangles* and *circles* denote MC and theoretical results, respectively. *Inset* shows a double-logarithmic plot of f_D against $\epsilon - \epsilon_c$ with $\epsilon_c = 1.67k_BT$, yielding a slope of 0.97 ± 0.02, in agreement with the prediction $f_D \propto (\epsilon - \epsilon_c)^{\nu/\phi}$. The *shaded area* shows the same phase diagram but derived in units of f (*right axis*) versus temperature T (*top axis*). It appears reentrant. Reprinted with permission from [60]

the intermolecular interactions [54, 55]. Much of the related upsurge of interest into the statics and dynamics of single macromolecules at surfaces has been spurred by the use of atomic force microscopy [56, 57] (AFM) and optical/magnetic tweezers [58], which allow one to manipulate single polymer chains. There is a close analogy between the forced detachment of an adsorbed polymer chain (such as polyvinylamine and polyacrylic acid) adhering to a solid surface (such as mica or a self-assembled monolayer) when the chain is pulled by the end monomer and the unzipping of homogeneous double-stranded DNA [59].

In our investigations [31, 60, 61] along with computer experiments we use the grand canonical ensemble (GCE) approach of Kafri et al. [59] in order to treat the detachment of a single chain from a sticky substrate when the chain end is pulled by external force (cf. Fig. 13a). A central result is the overall phase diagram of the force-induced desorption transition for a linear self-avoiding polymer chain (cf. Fig. 13b). We demonstrate its reentrant character when plotted in terms of detachment force f_D against system temperature T [31, 60]. We find that, despite being of first order, the force-induced phase transition of polymer desorption is dichotomic in its nature, that is, no phase coexistence and no metastable states exist! This unusual feature of the phase transformation is unambiguously supported by our simulation data, e.g., through the comparison of the order parameter probability distributions in the immediate vicinity on both sides of the detachment line, whereby no double-peaked structure is detected.

We obtained these results by studying the various conformational building blocks, characterizing the structure of an adsorbed linear polymer chain, subject to a pulling force of fixed strength. The GC partition function of the adsorbed chain of length N at fugacity z, $\Xi(z) = \sum_{N=0}^{\infty} \Xi_N z^N = V_0(z)Q(z)[1 - V(z)U(z)]^{-1}$, is

related to the GC partition functions $U(z)$, $V(z)$, and $Q(z)$ of loops, trains, and tails. Closed analytic expressions for the fraction of adsorbed segments (i.e., the order parameter of the desorption transition) and for probability distributions of trains, loops, and tails, cf. Eqs. (4) and (5), are derived in terms of the surface potential intensity both with and without external force. As an example, we refer here to the tail distribution without external force, which is given by:

$$
P_{\text{tail}}(l) = \begin{cases} \dfrac{1}{l^{\beta}} \exp\left[-c_1(\epsilon - \epsilon_c)^{1/\phi} \, l\right], & \epsilon > \epsilon_c \\[2ex] \dfrac{A_1}{l^{\beta}} + \dfrac{A_2 N^{1-\gamma_1}}{l^{\beta}(N-l)^{1+\phi}}, & \epsilon = \epsilon_c \\[2ex] \dfrac{N^{1-\gamma_1}}{l^{\beta}(N-l)^{1+\phi}}. & \epsilon < \epsilon_c \end{cases}
\tag{4}
$$

The same for the loop distribution reads:

$$
P_{\text{loop}}(l) = \begin{cases} \dfrac{1}{l^{1+\phi}} \exp\left[-c_1(\epsilon - \epsilon_c)^{1/\phi} \, l\right], & \epsilon > \epsilon_c \\[2ex] \dfrac{B_1}{l^{1+\phi}} + \dfrac{B_2 N^{1-\gamma_1}}{l^{1+\phi}(N-l)^{\beta}}, & \epsilon = \epsilon_c \\[2ex] \dfrac{N^{1-\gamma_1}}{l^{1+\phi}(N-l)^{\beta}}. & \epsilon < \epsilon_c \end{cases}
\tag{5}
$$

In Eqs. (4) and (5), A_1, A_2, B_1, and B_2 are constants and $\gamma_1 = 0.680$, $\beta = 1 - \gamma_1$ are universal exponents. Among other things, we verify the gradual transition of the PDF of loops from power-law to exponential decay as one moves away from the CAP to stronger adsorption. We demonstrate that for vanishing pulling force, $f \to 0$, the mean loop size, $L \propto (\epsilon - \epsilon_c)^{[1-(1/\phi)]}$, and the mean tail size, $S \propto 1/(\epsilon - \epsilon_c)^{1/\phi}$, diverge when one approaches the CAP. In contrast, for a non-zero pulling force, $f \neq 0$, we show that the loops on the average get smaller with growing force. Close to the detachment threshold, $f \approx f_D$, the tail length diverges as $S \propto \left(1 - \frac{f}{f_D}\right)^{-1}$. The simulation results for $P_{\text{tail}}(l)$, $P_{\text{loop}}(l)$ are in good agreement with the theoretical predictions. As expected, all these conformational properties and their variation with the proximity to the CAP are governed by a crossover exponent ϕ. An important result in this work is the calculation of ϕ, which provides insight into the background of the existing controversial reports about its numeric value. It is shown that the value of ϕ may vary within the interval $0.39 \leq \phi \leq 0.6$, depending on the possibility that a single loop interacts with the neighboring loops in the adsorbed polymer. Since this range is model-dependent,
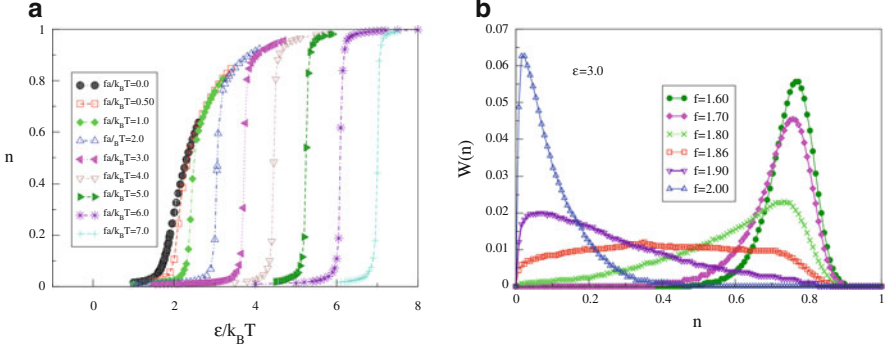
Fig. 14 (**a**) Order parameter (fraction of detached monomers) versus surface potential ϵ for different pulling forces. The chain is of length $N = 128$. (**b**) Order parameter distribution for pulling force $f\sigma/k_BT = 6.0$ and different adhesion energy ϵ/k_BT. The critical surface potential for this force is $\epsilon_D = 6.095 \pm 0.03$ so that the values $\epsilon/k_BT = 6.09$ and 6.10 are on each side of the detachment line. Reprinted with permission from [60]

one should not be surprised that different models produce different estimates of ϕ in this interval.

In Fig. 14a one can see the isotherms of the order parameter, $n = N_{ads}/N$, against the surface attraction ϵ for different pulling forces, f, which resemble closely those of a conventional first-order phase transition. However, as indicated by the corresponding PDF $W(n)$ (cf. Fig. 14b), the adsorption–desorption first-order phase transition under pulling force has a clear dichotomic nature (i.e., it follows an "either/or" scenario): in the thermodynamic limit $N \to \infty$ there is no phase coexistence! The configurations are divided into adsorbed and detached (or stretched) dichotomic classes. The metastable states are completely absent.

We would like to emphasize that our simulations have been carried out mainly within the framework of a constant-force ensemble, whereas one may also work in the constant-height ensemble whereby one uses the end-monomer height as an independent parameter and measures the force exerted by the chain on the end monomer, as we did in previous work [62]. Notwithstanding the equivalence of both ensembles, some quantities behave differently in each ensemble. So, for example, in the fixed-height ensemble one observes a constant-force plateau while the height of the chain end-monomer is varied. Most notably, the fraction of adsorbed monomers n varies steadily with changing h, whereas in the constant-force ensemble one observes a jump of n at a particular value of the force f. However, this should not cast doubt on the first-order nature of the phase transition, which can also be recovered within the constant-height ensemble, provided one expresses the control parameter h in terms of the average force $\langle f \rangle$. This interesting aspect has been considered in detail by Skvortsov et al. [63].

Last but not least, we would like to point out a very recent investigation [64] in which we show that the change of detached monomers with time is governed by a differential equation that is equivalent to the nonlinear porous medium equation,
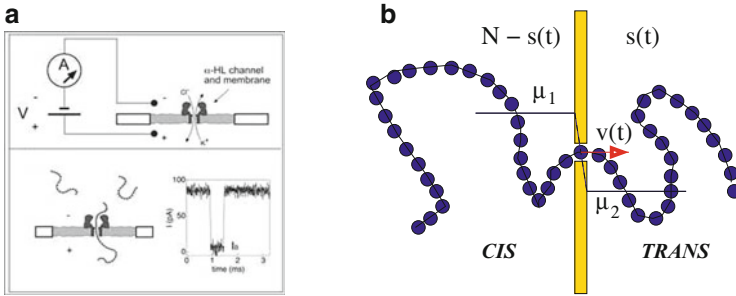
Fig. 15 (**a**) DNA translocation through a protein pore in α-hemolysin. When the DNA enters the pore, the ionic current is blocked. This current blockage is used to detect the residence time of DNA bases in the pore [67]. (**b**) Chain translocation through a nanopore. The instantaneous translocation coordinate is $s(t)$ and the bead velocity in the pore is $v(t)$. The driving force is due to a chemical potential gradient within the pore, $f = (\mu_1 - \mu_2)/k_BT$. Adapted from [68]. Reproduced by permission of IOP Publishing. All rights reserved

employed widely in transport modeling of hydrogeological systems. Depending on the pulling f and restoring φ forces, one can discriminate between a "trumpet" ($1/N^\nu \ll \varphi < f < 1$), "stem-trumpet" ($\varphi < 1 < f$), and "stem" ($1 < \varphi < f$) regimes of desorption. Remarkably, in all these cases the time dependence of the number of desorbed monomers $M(t) = N - N_{ads}(t)$ and the height of the end monomer (i.e., the monomer that experiences the applied external pulling force) $h(t)$ follow an universal $\sqrt{t}$ – law (even though this is not a diffusion phenomenon). There is, however, a common physical background with the well-known Lucas–Washburn $\sqrt{t}$-law of capillary filling [65], as with the ejection kinetics of a polymer chain from a cavity (virus capsid) [66]. In these seemingly different phenomena there is always a constant driving force (meniscus curvature or polymer entropy) that acts against a gradually changing drag force (friction) in the course of the process.

1.5.2 Polymer Translocation Through Narrow Pores in the Membranes and Escape from Long Pores

The translocation of a polymer is the process during which a flexible chain moves through a narrow pore of size comparable with that of a chain segment to go from one (*cis*) side of a membrane to the other (*trans*) side, as shown in Fig. 15. This phenomenon is important in many biological and chemical processes, such as viral injection of DNA into a host and RNA transport through a nanopore of the nuclear membrane, and appears highly promising as a possible nanotechnological application, e.g., for drug delivery [67, 69], rapid DNA sequencing [67, 70, 71], gene therapy, etc.

During the last decade, polymer translocation has thus turned into a very active area of research with a variety of theoretical, simulational, and experimental studies examining this process under different conditions [68]. Different driving

mechanisms for the translocation processes have been a subject of intense discussion, e.g., electric fields [72], chemical potential gradients [73], selective adsorption on one side of the membrane [74, 75], and related ratchet mechanisms [76]. In addition, entropic barriers, segment crowding at the pore orifice, and, most notably, the interplay between topological connectivity of the chain and geometric constraints imposed by the pore, make the problem rather intricate and complex. Moreover, since polymer translocation is such an ubiquitous phenomenon, it remains questionable whether a single universal scenario is operative under all circumstances, so detailed studies of its various aspects are necessary.

It is convenient and customary to describe the translocation process by a single variable s, called the translocation coordinate, which denotes the sequential number of the monomer located in the pore at time t, and tells how much of the polymer has passed meanwhile through the pore (cf. Fig. 15b). As a rule, once the initial monomer has already threaded through the hole, among the principal quantities of interest are the mean translocation time τ, and its dependence on polymer length N and on the driving force magnitude f. In fact, τ is one of the few dynamic quantities that are accessible in current experiments [67, 70, 71]. Assuming that $\tau \propto N^{\alpha} f^{-\delta}$, one of the objectives is to provide a plausible explanation for the observed values of the exponents α and δ. Important information is obtained from the probability distribution function of translocation times, $Q(t)$, and also from the time dependence of the mean squared displacement (variance) of the translocation coordinate $\Delta(t) \equiv \langle \Delta s^2(t) \rangle = \langle s^2 \rangle - \langle s \rangle^2$. Both quantities play essential roles in numerous efforts to elucidate a typical hallmark of the translocation process. Namely, its dynamics is anomalous with $\langle \Delta s^2(t) \rangle \propto t^{\beta}$, where $\beta < 1$ (i.e., the dynamics is subdiffusive) for the force-free (i.e., $f = 0$) case and $\beta > 1$ (i.e., super-diffusive) for the force-driven polymer translocation. This is well established at present [77–80].

There are different possibilities for how the forced translocation can be effected. For example, Milchev at al. [74, 75] studied the possibility that the monomer–membrane interaction is attractive on the *trans* side, while it is assumed to be repulsive on the *cis* side. Assuming that a few monomers of a chain have already passed through the pore and experience the favorable membrane–monomer interaction on the *trans* side, two questions that are asked are: (1) How likely is it that the rest of the chain will follow from the *cis* to the *trans* side, depending on chain length N and the distance $T/T_c - 1$ from the adsorption transition that happens on the *trans* side at $T = T_c$? (2) How does the time needed for complete translocation depend on these parameters?

Milchev et al. [74, 75] found that it makes a big difference whether one studies the case in which in equilibrium a chain is not yet absorbed on the *trans* side (and still in a mushroom state when the chain gets through the pore) or whether adsorption occurs. In the first case, the problem is similar to unbiased translocation (which occurs by thermal fluctuations only [81, 82]), i.e., for any finite fraction of monomers that have already passed to the *trans* side there is still a non-zero probability that the whole chain returns to the *cis* side (and diffuses away). In this case, the translocation time is found to scale as $\tau \propto N^{2\nu + 1} \approx N^{2.2}$, i.e., the time is simply of the order of the Rouse time of a single chain in a good solvent (note that the Monte Carlo modeling of Milchev et al. [74, 75] uses implicit solvent

and there cannot be any effects due to hydrodynamic interactions). In any case, this result already shows that the relation $\tau \propto N^2$ [81, 82] (derived on the assumption that the problem can be reduced to a quasi-one-dimensional problem of diffusion over an entropic barrier, taking the numbers of monomers at the *trans* side as "reaction coordinate") cannot hold in general. Indeed, Dubbeldam et al. [77, 78] have shown that different power laws can be obtained by a model in which ordinary diffusion is replaced by fractional Brownian motion, which leads to anomalous diffusion.

When one studies translocation driven by adsorption for temperatures where in equilibrium the chain is adsorbed on the *trans* side in a "pancake configuration," one finds that a finite number of monomers adsorbed on the *trans* side (of order 10) suffices to pull the remaining chain through the hole in the membrane in almost all cases. The relaxation time was found to scale like $\tau \propto N^{1.7}$, but is not clear whether this exponent can be theoretically explained [74, 75].

The standard model for forced translocation uses a biasing force on any monomer that has entered the pore, driving it from the *cis* to the *trans* side (see [83] and references therein). Estimates for the various exponents describing the translocation dynamics have been given [83], but in this study (as well as in other work that can be found in the literature) it is not clear whether the asymptotic scaling regime really has been reached or whether one observes "effective exponents" due to slow crossovers. In addition, a rather fundamental problem [83, 84] is a strong conformational asymmetry of the part of the chain that is still on the *cis* side and the part that is already on the *trans* side: the former part is under stretch because parts of the chain very distant (along the contour) from the pore have not yet relaxed. Translocation happens too fast for the chain configurational degrees of freedom to reach local equilibrium. So, the radius of the *cis* part is relatively too large.

Conversely, the configuration of the *trans* part is somewhat too dense and, hence, the radius is too small [83, 84]. Although some aspects of this phenomenon have been discussed by Sakaue [85, 86], we feel that a complete theory of translocation that properly incorporates all these out-of-equilibrium effects still needs to be developed.

In the wake of these developments, our studies of translocation dynamics have been focused on the generic case of unbiased translocation [77, 79, 80] in the absence of driving force, $f = 0$, and on the case when the chain threading through a pore is driven by applied force [78, 87–89]. In our original efforts to capture the essence of the problem, we employed diverse methods (scaling theory, fractional calculus, Monte Carlo and molecular dynamics simulations). We found that the relevant dynamic variable, the transported number of polymer segments s (t), displayed an anomalous diffusive behavior both with and without an external driving force being present [77–80]. A closed analytic expression for the probability, $W(s, t)$, of finding s translocated segments at time t in terms of chain length N and applied drag force f was derived from the fractional Fokker–Planck equation and shown to provide analytic results for the time variation of the statistical moments $\langle s(t) \rangle$ and $\langle s^2(t) \rangle$. It was shown that in the absence of driving force, the time τ needed for a macromolecule of length N to thread from the *cis* into
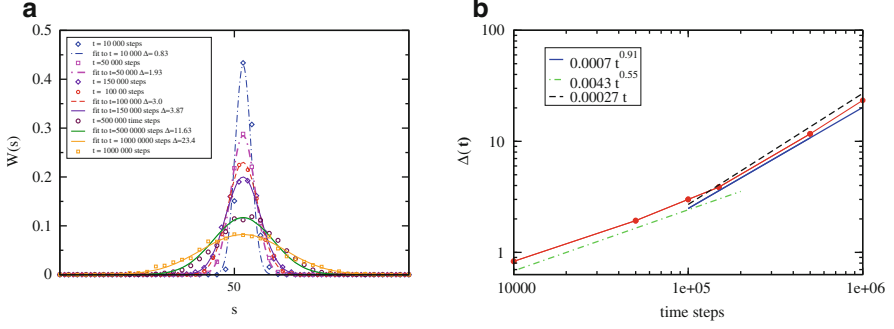
Fig. 16 (**a**) The probability distribution of translocation coordinate $W(s, t)$ at five different time moments (*symbols*) along with Gaussian fits (*lines*) with variance Δ. (**b**) Increase of the variance $\Delta(t)$ with elapsed time t, indicating a crossover from short-time subdiffusive behavior $\propto t^{0.55}$ to late time nearly normal diffusive behavior $\propto t^{0.91}$. Reprinted with permission from [87]

the *trans* side of a cell membrane scales like $\tau \propto N^{2\nu+2-\gamma_1}$ with the chain length. Thus, the anomalous dynamics of the translocation process has been related to a universal exponent that contains the basic universal exponents of polymer physics, the Flory exponent ν, and the surface entropic exponent γ_1. If a driving force is present, our results suggested a scaling $\tau \propto f^{-1}N^{2\nu+1-\gamma_1}$, in good agreement with Monte Carlo (MC) and molecular dynamics (MD) simulation data.

While validating the sub- or superdiffusive behavior of $\langle \Delta s^2(t) \rangle$, several new findings revealed that the probability distribution of the translocation coordinate s, i.e., $W(s, t)$, stays Gaussian for different time moments. Moreover, the long time tail of the translocation time distribution was found to have an exponential form, challenging the power-law behavior [77, 78] predicted within the fractional Fokker–Planck equation. In an effort to reconcile the new findings with the observed sub- or superdiffusive variation of $\Delta(t) = \langle \Delta s^2(t) \rangle$, we recently suggested a new governing equation [87, 88], based on the fractional Brownian motion (fBm) approach (cf. Fig. 16 for the force-free case).

Starting from the Langevin equation $ds(t)/dt = v(t)$ where, by assumption, the translocation velocity $v(t)$ follows Gaussian statistics, we derived a Fokker–Planck equation for the distribution $W(s, t)$:

$$\frac{\partial}{\partial t} W(s, t) = - \frac{\partial}{\partial s} [K(s) \, W(s, t)] + \mathcal{D}(t) \, \frac{\partial^2}{\partial s^2} \, W(s, t) \qquad (6)$$

where the average velocity is $\langle v(t) \rangle \equiv K(s)|_{s \, = \, s(t)}$ and the time-dependent diffusion coefficient $D(t) = \int_0^t G(t, t') dt'$, with G being the second moment (velocity autocorrelation function) $G(t_1, t_2) \equiv \langle [v(t_1) - \langle v(t_1) \rangle][v(t_2) - \langle v(t_2) \rangle] \rangle$, assuming a (constant) friction coefficient, ξ_0. In the simplest case of the unbiased process (i.e., $f = 0$), Eq. (6) can be solved to:
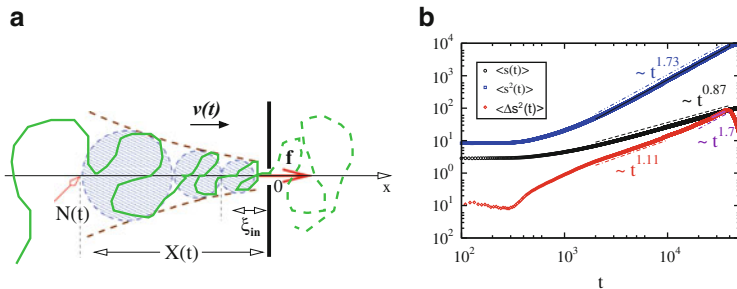
Fig. 17 (**a**) Dynamic response of a driven polymer translocation upon switching the pulling force f. At time t the tension force has passed the $N(t)$ monomer and is at distance $X(t)$ from the membrane while $M(t)$ monomers have already moved into the *trans* side of the separating membrane. The chain portion to the *right* of $X(t)$ is moving with mean velocity $v(t)$. (**b**) First and second moments of the translocation coordinate $\langle s \rangle$ and $\langle s^2 \rangle$, and the variance $\langle \Delta s(t)^2 \rangle = \langle s^2 \rangle - \langle s \rangle^2$ for a polymer chain with length $N = 100$ and driving force $f = 5.0$. Reprinted with permission from [89]

$$W(s,t) = \frac{1}{\sqrt{2\pi D t^\beta}} \, \exp\left[-\frac{(s - s_0)^2}{4 D t^\beta} \right] \tag{7}$$

where D is a constant. Therefore, the distribution $W(s, t)$ is indeed Gaussian, albeit with a width proportional to the variance $\Delta(t)$ (cf. Fig. 16), which in this case follows a subdiffusive behavior (i.e., $\beta < 1$). This result reproduces the MC simulation findings reported recently by Kantor and Kardar [90].

In an effort to lean on a solid physical background in order to describe faithfully the more complex (far from equilibrium) case of a driven translocation, following the pioneering work of Sakaue [85, 86], we considered the propagation of a tensile front along the polymer chain backbone upon pulling [89]. As shown schematically in Fig. 17a, when a pulling force is instantaneously switched on, tension starts to propagate along the chain backbone and progressively alters the polymer conformation. Eventually, after some characteristic time, a steady state is reached and the whole polymer starts moving with constant velocity. We find that:

- The translocation starts with the formation of initial Pincus blob (i.e., the first blob is generated immediately at the pore entrance). The characteristic time for blob initiation is given by $\tau_{\text{init}} \propto a\xi_0/f$. Our MD simulation results essentially support the scaling prediction $\tau_{\text{init}} \sim 1/f$.
- The initiation is followed by a tensile force transmission along the chain backbone that is governed by the local balance of driving and drag forces. For forces in the interval $N^{-\nu} \ll af/k_B T < 1$ this leads to the so-called trumpet regime (see Fig. 17a). The corresponding translocation time is given by $< \tau > \propto C_1 f^{1/\nu - z + 1} N^{1 + \nu} + C_2 f^{2 - z} N^{2\nu}$, where the dynamic exponent $z = 2 + 1/\nu$ for Rouse dynamics and $z = 3$ for Zimm dynamics. C_1 and C_2 are numerical model-dependent constants. As a result, different scaling of τ is observed,

depending on chain length N and driving force strength f. Thus, one expects a crossover from $N^{2\nu}/f^{1/\nu}$ to $N^{1+\nu}/f$, i.e., the translocation exponent α grows with increasing force f from $\alpha \approx 1.18$ to $\alpha \approx 1.59$.

- For strong forces, the translocation time can be estimated as $<\tau> = C_1 \tau_0 N^{1+\nu}/\widetilde{f}_a + C_2 \tau_0 N^{2\nu}/\widetilde{f}_a$ where the first term dominates under condition $N^{1-\nu} \gg C_2/C_1$. Therefore, the translocation scaling exponent grows from $\alpha = 2\nu$ to $\alpha = 1 + \nu$ as the chain length N increases. This is in agreement with the results of MD and MC simulations. A scaling relation very close to $\langle\tau\rangle \propto N^{2\nu}/\widetilde{f}_a$ has been found experimentally [91] in the case of translocation of long double-stranded DNA through a silicon oxide nanopore. In this experiment the translocation exponent was $\alpha = 1.27$, which is close to our theoretical prediction.

- Even if the mentioned approach appears to yield physically plausible and qualitatively correct results, generally, the MD simulation findings yield systematically smaller values for the translocation exponent, e.g., $\alpha \approx 1.11$ and $\alpha \approx 1.47$ for weak and strong forces, respectively. As we show below, this shortcoming of the theory stems most probably from neglecting the role of fluctuations during the translocation process, which is common to most theoretical treatments so far.

In our most recent work, we investigated the impact of thermal fluctuations on the driven translocation dynamics, theoretically and by means of extensive MD simulation [88]. Indeed, the role of thermal fluctuations is by no means self-evident. Our theoretical consideration is based on the Fokker–Planck equation (FPE) Eq. (6), which has a nonlinear drift term and a diffusion term with a time-dependent diffusion coefficient $\mathcal{D}(t)$.

Our MD simulation reveals that the driven translocation process follows a superdiffusive law with a running diffusion coefficient $\mathcal{D}(t) \propto t^\gamma$, where $\gamma < 1$. Therefore, although in the unbiased translocation case, the diffusion is Brownian (or slightly subdiffusive), in the biased regime the process becomes superdiffusive, i.e., the variance $\langle\Delta s^2\rangle \propto t^\theta$, where $1 < \theta < 2$ (cf. Fig. 17b). Moreover, the exponent θ increases with the growth of the driving force f, namely, $\theta = 1.5$ for $f = 1$, and $\theta = 1.84$ for $f = 10$. This finding is then used in the numerical solution of the FPE, which yields an important result: for comparatively small driving forces, fluctuations facilitate the translocation dynamics. As a consequence, the exponent α, which describes the scaling of the mean translocation time $\langle\tau\rangle$ with the length N of the polymer, $\langle\tau\rangle \propto N^\alpha$, is found to diminish. Thus, taking thermal fluctuations into account, one can explain the systematic discrepancy between the theoretically predicted duration of a driven translocation process, considered usually as a deterministic event, and measurements in computer simulations.

Finally, a related interesting problem occurs when a force acts on a chain end of a flexible macromolecule, which is dragged into a nanotube with repulsive walls (Fig. 18). Since in a nanotube of diameter D, the chain (under good solvent conditions) forms a string of blobs, $g \propto N^{1/\nu}$ monomers per blob, and each blob costs a free energy of $k_B T$, there is a free energy cost of order $N/g \propto N D^{-1/\nu}$ that needs to be overcome by the force. Klushin et al. [92] showed, by a phenomenological scaling

Fig. 18 Flexible polymer chain with one end dragged into a nanotube in a quasi-equilibrium process. The coordinate x of the end where the force acts is taken as a reaction coordinate. At $x = x^*$ the free part of the chain is suddenly sucked into the nanotube. Reprinted with permission from [92]. Copyright 2008 American Chemical Society
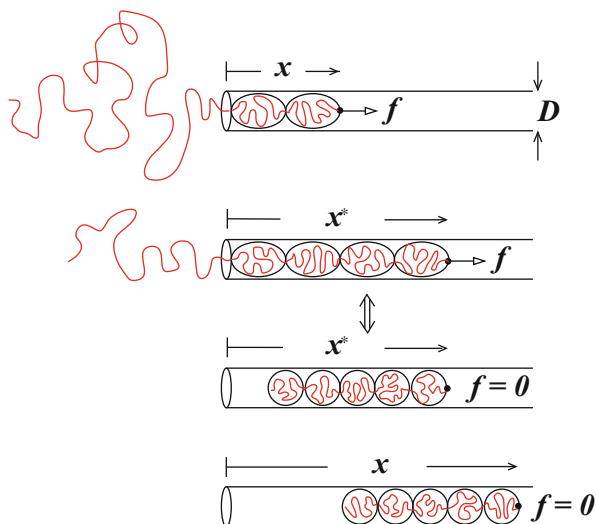
theory and by simulation, that the process has discontinuous features: after a critical fraction of the chain is drawn into the tube, the rest moves into the tube, releasing the tension that is still present as long as part of the chain is still outside the nanopore.

2 Reversible Kinetics of Hydrogen-Bond Networks

The discussion so far has focused on the general properties of single polymer chains, but in many applications and experimental realizations of the forced desorption or unfolding of biomolecules the specific nature of the adhesion bonds under study determine specific material properties. In many situations, one is confronted with an adhesion cluster that is stabilized by a number of parallel bonds. One important class of noncovalent adhesion bonds is provided by hydrogen bonds (H-bonds). The most common situation that is encountered in many experimental investigations of the mechanically forced opening of adhesion bonds via dynamic force spectroscopy (DFS) employing atomic force microscopes or optical tweezers is the following: The system under study consists of adhesion complexes that are pulled in order to investigate the rupture events. Often, the rupture event is irreversible in the sense that reversing the pulling direction does not give rise to rebinding. Recently, reversible bond breakage has also been studied in different systems [93, 94] and one particular study will be reviewed in the following section (Sect. 2.2) [95]. In Sect. 2.1, we will report on the results of force probe MD simulations on dimers of calix[4]arene catenanes that show very interesting reversible H-bond network dynamics. In addition, we briefly review the theoretical treatment of the stochastic dynamics of reversibly binding systems under different protocols of external force application.
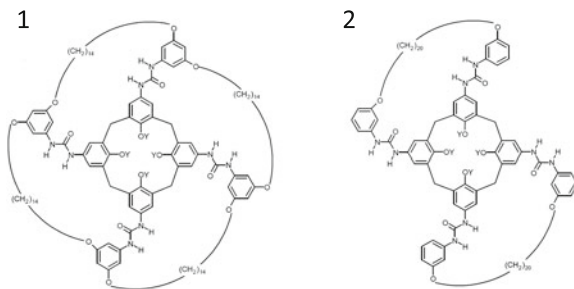
Fig. 19 Structure of the calix[4]arene monomers. Note the shorter loop length in the tetra-loop (**1**) compared to the bis-loop (**2**) system. *Y* indicates CH_3. Reprinted with permission from [98]. Copyright (2011) American Chemical Society

2.1 Force Probe MD Simulations of Calix[4]arene Catenanes

Catenanes constitute a family of molecules that are interesting because of their potential incorporation into molecular motors or switches [96] and, in particular, the specially designed calix[4]arene catenanes that have been synthesized recently have interesting properties [97]. We have investigated exactly the same systems that are also the subject of experimental DFS investigations reviewed in Sect. 3, namely dimers of two calix[4]arenes with the structures presented in Fig. 19 [98] using mesitylene as an aprotic solvent. Structure **1** has four aliphatic loops of 14 CH_2 groups and structure **2** has two longer loops consisting of 20 CH_2 groups. In the dimers, the loops are intertwined building catenane structures, which in equilibrium form a compact aggregate stabilized by 16 H-bonds formed between urea groups located at the upper rim of the calixarene monomers (UU-bonds). If one pulls the dimer along the direction connecting the calixarene "cups," this compact structure opens but the monomers cannot dissociate completely due to the mechanical lock provided by the intertwined loops. These systems therefore are ideally suited for a study of reversible binding. All force probe MD simulations were performed in the so-called force ramp mode, meaning that the force increases linearly with time, $F(t) = k_c \cdot v \cdot t$, with the pulling velocity v and the stiffness of the pulling device k_c. These simulations reveal that, after opening the compact structure, a new set of H-bonds forms between the urea groups of one monomer and the ether groups of the other monomer (UE-bonds). In the system with four loops, this structure cannot be opened by further pulling the system because of the rather short loop length. In Fig. 20, the structure of the closed and open configuration of the tetra-loop system is shown along with a sketch of the H-bonds present in the respective states. The pulling direction in the force probe MD simulation is indicated by the arrow in the closed structures shown in the upper part of Fig. 20.

If one reverses the pulling direction after the system has undergone the transition to the open structure, one observes a rebinding into the closed state for pulling
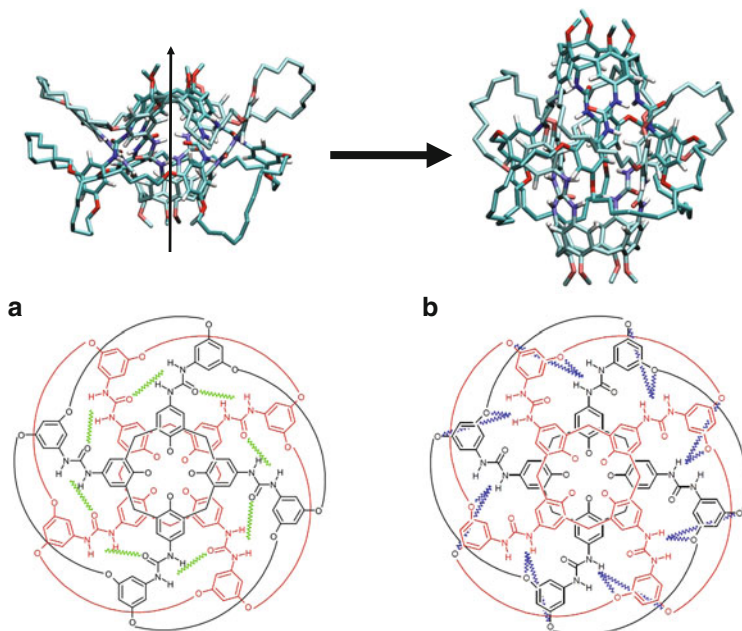
Fig. 20 *Top*: Examples of the configurations of the (**a**) closed ($t = 0$) and (**b**) open ($t = 17$ ns) structures of the tetra-loop system from a pulling simulation with $v = 0.1$ nm/ns. *Bottom*: Representations of the tetra-loop calix[4]arene dimer. The loops consist of 14 CH_2 groups; the endstanding CH_3 groups linked to the oxygen atoms are not shown. (**a**) UU-bonds relevant in the closed state are indicated in *green*. (**b**) UE-bonds stabilizing the open state are drawn in *blue*. Reprinted with permission from [98]. Copyright (2011) American Chemical Society

velocities v that are not too large. This is exemplified in Fig. 21, which shows typical force versus extension curves for the tetra-loop system calculated for different pulling velocities. The hysteresis hallmarking the nonequilibrium nature of the simulations is evident immediately. From the dependence of the hysteresis on the pulling velocity it becomes clear that the system will not rebind for large v if the force is relaxed after the opening transition. Thus, if one considers the time scale set by v, the system appears irreversible on a fast time scale and reversible on a slower time scale.

Because the rupture event is a stochastic process, the rupture forces are distributed in a certain range. Therefore, as in the experimental studies, we performed a large number of simulations and analyzed the rupture force distributions and the rejoin force distributions. The mean values as a function of the pulling velocity represent the so-called force spectrum. Experimentally, often a logarithmic dependence of the mean rupture force on v is observed, but the data collected by Schlesier et al. [98] allow no definite conclusion regarding this dependence.

As mentioned above, we also performed simulations on a bis-loop system undergoing two transitions. The first transition is from a compact, closed structure stabilized by a maximum of 16 UU-bonds to an intermediate reminiscent of the open structure of the tetra-loop system. In the second transition, this UE-stabilized structure opens upon further increase of the external force and an open structure
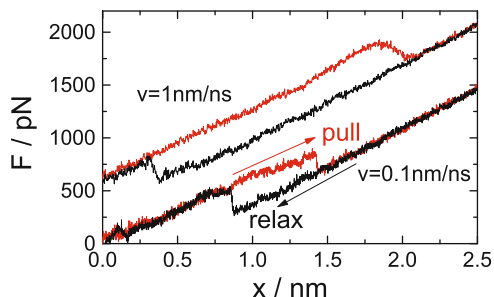
Fig. 21 Representative force versus extension ($x = v \cdot t$) curves for the tetra-loop system for the pull mode (*red*) and the relax mode (*black*). The *upper curves* are for $v = 1$ nm/ns ($v = -1$ nm/ns in the relax mode) and are shifted by 600 pN for clarity. The *lower curves* are for $v = 0.1$ nm/ns ($v = -0.1$ nm/ns). Reprinted with permission from [98]. Copyright (2011) American Chemical Society
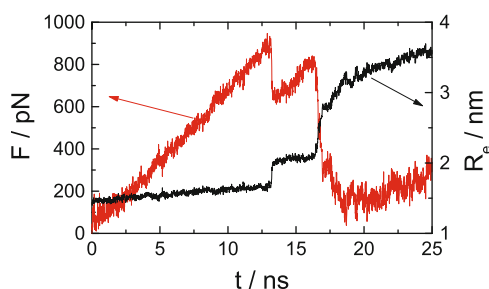
Fig. 22 Measured force $F = k \cdot q$ and R_e for the bis-loop system as a function of simulation time for $v = 0.1$ nm/ns for a representative simulation run. Reprinted with permission from [98]. Copyright (2011) American Chemical Society

devoid of any H-bonds forms. In this structure, the dimer cannot dissociate completely due to the mechanical lock imposed by the aliphatic loops. Figure 22 shows the measured force F and the end-to-end distance, R_e, as a function of simulation time for the system along the arrow shown in Fig. 21. The two steps in the force with the concomitant step-like increase in the end-to-end distance are clearly visible. In contrast to the tetra-loop system, the bis-loop system shows only irreversible opening of the structures and no rejoining for the pulling velocities used in the simulations. However, an analysis of the life-time of the intermediate state revealed that this structure might well be of relevance for the interpretation of the experiments.

All simulations discussed so far have been performed using one particular force field, the GROMOS G53A5 force field [99]. Because it is well known that the choice of the force field has a strong impact on the results of MD simulations, we performed force probe MD simulations of the tetra-loop calix[4]arene dimer using three different frequently used force fields [100]. The most important

conclusion to be drawn from a comparison of the GROMOS G53A5, OPLS−AA [101], and AMBER GAFF [102] force fields is that there are only quantitative differences in the results regarding rupture forces, rebinding ability, and structural quantities. Thus, the fact that one imposes quite strong nonequilibrium conditions on the system does not give rise to additional problems in MD simulations (at least for the force fields studied).

2.2   Stochastic Modeling of Reversible Bond Breakage

As discussed above, the reversible opening of adhesion bonds or the reversible unfolding of biomolecules has been investigated in the recent past with increasing intensity. The fact that both the opening and the rejoining events can be observed in favorable examples opens the way to more detailed information regarding the energy landscape of the system under study. The analysis of experimental DFS data showing irreversible rupture events is usually based on the phenomenological Bell model [103]. In this model, it is assumed that the application of an external force F to the system results in a decrease in the activation energy for bond rupture, E_A, by an amount $(F \cdot x)$. Here, x denotes the distance from the free energy minimum of the closed structure to the transition state. Thus, the escape rate simply reads as $k(F) = k_0 e^{\beta F x}$ ($\beta = 1/T$ with the Boltzmann constant set to unity). Assuming first-order kinetics for the escape from the closed state, one can calculate the rupture force distribution if the time-dependence of the force, $F(t)$, is known.

The time-dependence of the force is determined by the protocol applied in the actual application of DFS. One common way to perform the experiments or simulations is the force-ramp mode, in which the applied force increases with a constant velocity, $F(t) = k_c \cdot v \cdot t$, where k_c denotes the force constant of the pulling device. The other protocol, called force-clamp mode, consists in the application of a constant external force, $F(t) = F_{ext}$. In the force-ramp case, one finds the logarithmic dependence of the mean rupture force and v quoted above. The simple model appears to work quite well for small pulling velocities but fails if one pulls fast. In this situation, more detailed calculations of the rupture force distributions via the computation of the mean first passage time in model free-energy landscapes give more reliable results [104].

The impact of reversible rebinding on the rupture force distributions has been investigated only recently [105, 106] and showed that one reaches equilibrium between the closed and open structure for vanishing pulling velocity and gave the results of the Bell model for fast pulling. We have analyzed the behavior of both the rupture force and rejoin force distributions for the stochastic dynamics in a double-well potential and have considered the dependence of the shape of the distributions and the mean forces on system parameters such as the pulling device stiffness k_c for the force-ramp protocol [107] (cf. Fig. 23). It was shown that it should be possible to extract the equilibrium constant defined by the kinetic rates for bond rupture and rejoining from the equilibrium forces, i.e., the mean forces obtained in the limit of
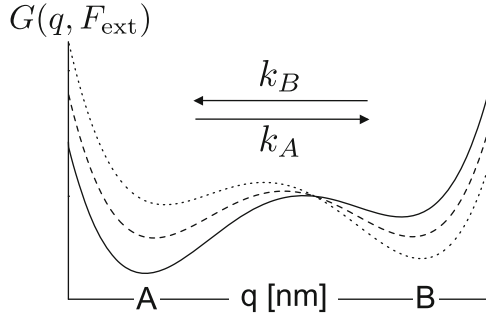
Fig. 23 Free energy $G(q, F_{ext})$ as a function of the reaction coordinate defined as the pulling direction for various values of the applied force. For larger applied force, the *right-hand* "B" minimum becomes deeper (*dashed* and *dotted lines*) and the equilibrium constant $K(F_{ext})$ decreases. Reprinted with permission from [108]. Copyright 2010 by the American Physical Society

vanishing pulling velocity. Also, the impact of a soft worm-like chain (WLC) polymeric linker has been treated in an approximate manner using an effective compliance of the composite system. It was found that not only the rupture force distribution but also the rejoining force distribution is affected in a specific way, depending on the parameters of the WLC model. Given the fact that the WLC model might fail (cf. the discussion on this point in Sect. 1.2), this can be of importance when analyzing DFS experiments. Additionally, it was found that in equilibrium the impact of the linker on the equilibrium rupture forces vanishes. This finding, however, depends on the specific model used to treat the system composed of the double-well potential and the linker.

If the reversible dynamics of bond rupture is considered in the force clamp mode, one can exploit an analogy to the treatment of single molecule fluorescence to treat the statistical properties of the transition events [108, 109]. If one considers two states, A (closed) and B (open) with rates $k_A = k(A \rightarrow B)$ and $k_B = k(B \rightarrow A)$, the equilibrium constant is given by $K = k_B/k_A$. Due to the strong exponential dependence of the kinetic rates on the external force, in the Bell model given by $k_A(F) = k_A e^{\beta F \cdot x_A}$ and $k_B(F) = k_B e^{-\beta F \cdot x_B}$ one can vary K over a broad range. This fact opens the possibility of very detailed analysis of two-state kinetics. In particular, an analysis of the Mandel parameter [109] and the waiting time distributions [108] should allow the investigation of deviations from simple Markovian kinetics. Different event counting schemes can be utilized, depending on the value of the equilibrium constant, in order to study the possible effect of dynamic or static disorder on the kinetics. As shown in Fig. 24, in the so-called cycle counting scheme only B→A transitions are counted, and in the event-counting scheme every transition is considered. In particular, in situations where K differs strongly from unity, the cycle-counting scheme may be advantageous due to resolution problems. In favorable cases, an analysis of the moments of the corresponding waiting times will allow deciding whether the system can be described as a two-state system or whether a more complex scheme is required for successful modeling of the kinetics.
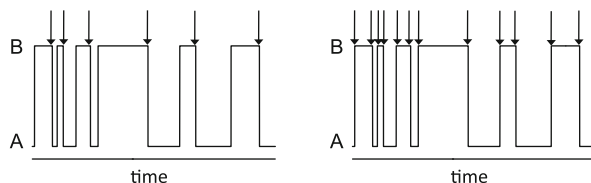
Fig. 24 Example trajectories showing the two different ways of counting, as indicated by the *arrows*. *Left*: cycle-counting (only B→A transitions are counted), *Right*: event-counting (all transitions are counted). Reprinted with permission from [108]. Copyright 2010 by the American Physical Society

3 Force Spectroscopy and Microscopy of Modular Macromolecules

With the advent of nanotechnology, there has been a strong increase in interest in the physics of small systems far from equilibrium. Mechanically driven transformations, as carried out by single-molecule stretching experiments or observed for molecular machines, offer a unique way to study fundamental theories of statistical mechanics associated with fluctuation-dissipation theorems. Here, we describe the mechanics of unfolding fibronectin in the presence of osmolytes as a model for proteins present in the extracellular matrix. Stretching of single proteins is done by force spectroscopy, giving insight into the structure of fibronectin. We found that preferential exclusion of osmolytes enhances the stability of proteins. Furthermore, we describe the mechanics of oligo calix[4]arene catenanes as a model system that permits the control of the spatial boundaries for separation of hydrogen bonds by mechanically arresting the unbound state with tailored loop entanglement. Thereby, we can investigate hydrogen bond breakage both close to equilibrium and also far from equilibrium by adjusting the separation velocity using a linear force ramp. The loops permit the reversible rupture and rejoining of individual nanocapsules. Experiments carried out by force spectroscopy using an atomic force microscope are backed up by MD simulations and stochastic modeling and reveal the presence of an intermediate state between the closed and open state of a single nanocapsule.

3.1 Preferential Exclusion of Ectoin Enhances the Mechanical Stability of Fibronectin

Production of osmolytes plays a pivotal role in the adaptation of organisms to high salt conditions. Compatible solutes may act as stabilizing agents, which protect cells from denaturing [110–113]. Among the various compatible solutes, ectoine (1,4,5,6-tetrahydro-2-methyl-4-carboxylic acid; Fig. 25), a zwitterionic
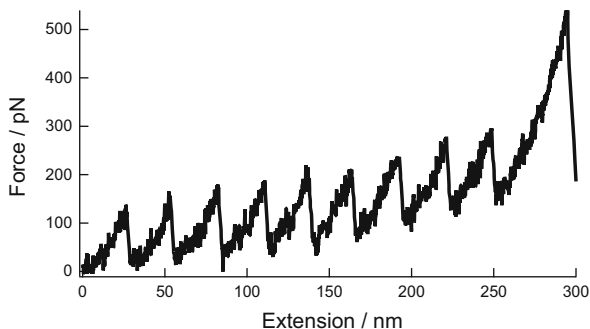
Fig. 25 Chemical structure of ectoine
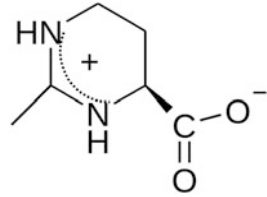
cyclic amino acid, is the most common solute found in the cytosol of aerobic heterotrophic bacteria where it increases the thermotolerance [114, 115]. In general, it has been suggested that the presence of osmolytes increases the stability of proteins and preserves enzymatic activity in an aqueous environment. These properties make the compounds potential candidates for biotechnological applications ranging from food processing to protection of tissue from environmental stress factors such as UV irradiation [116]. Timasheff and coworkers [117] argue that the main factor in stabilizing protein structure by large quantities of osmolytes dissolved in water originates from the increase in surface tension of the water, thus leading to a preferential exclusion of the osmolytes from the protein–water interface. The increase in surface tension is in accordance with Gibbs' isotherm and forces the protein to adopt a more compact protein structure that reduces the surface area exposed to the aqueous phase without perturbing its native function.

Intrigued by this mechanism of protein stabilization, we wanted to prove this hypothesis of protein stabilization by employing single-molecule stretching experiments using proteins. We deliberately chose proteins from the extracellular matrix because they would be exposed to external stresses in the most profound way. AFM and particularly single-molecule force spectroscopy can provide insights into the stability of single ligand–receptor pairs and the elastic properties of individual macromolecules [118–120]. Besides stretching of simple homopolymers, a variety of different biological macromolecules ranging from polysaccharides to modular proteins such as titin and spectrin have been investigated by means of force–extension curves [118, 121, 122]. Most of the pioneering work in this area stems from the group of Gaub and coworkers [123, 124]. Force-induced unfolding of proteins is particular interesting for unraveling the structure–function relationships of protein filaments involved in the mechanical function of cells and extracellular matrix. Stretching of modular proteins such as titin [123], tenascin [125], spectrin [126], and fibronectin [127] at different loading rates can be used to gather information about the energy landscape of the folded structure. Thereby, Müller and coworkers [128] were able to remove individual domains of single bacteriorhodopsin molecules from a solid supported membrane, giving unfolding fingerprints displaying the structural integrity of the protein under investigation [129].

Previously, we were able to measure the mechanical unfolding of single native fibronectin to reveal the detailed composition of the protein, known to consist

of three types of subunits FN-I, FN-II, and FN-III that differ in the number of amino acids (45, 60, and 90, respectively) [127]. Fibronectin contains 220 kDa subunits linked into dimers and polymers by disulfide bonds. Fibronectin binds to the cell surfaces via integrins and other extracellular molecules, thereby mediating cell adhesion [130]. Stretching of the molecule results in a subsequent unfolding of the globular domains FN-I, FN-II, and FN-III, which all adopt a beta-sandwich structure. Each unfolding event is accompanied by a specific lengthening of the filament, which corresponds to the number of amino acids forming an individual subunit. This complete and subsequent noncooperative unfolding of subunits results in a typical sawtooth pattern of the force–extension curve (Fig. 26). Evans and Ritchie found that the force of each subsequent unfolding event rises by a constant factor due to simple statistical reasons [132].

Here, we report on single-molecule stretching of native fibronectin and the influence of the compatible solutes ectoine and sarcosine on the mechanical properties, as revealed by the unfolding of the individual subunits and the overall persistence length of the macromolecule [131]. In accordance with the preferential exclusion model, we found a significant stabilization of the protein structure in the presence of osmolytes but not an increase in unfolding forces.

3.1.1 Stretching of Native Fibronectin

Figure 26 shows a typical force–extension curve of a single native fibronectin dimer stretched in between a force probe such as an AFM tip and the substrate. Analysis of the force–extension curves is simplified by the fact that the subunits unfold independently from each other, whereas the individual unfolding process of a single protein domain is entirely cooperative and occurs as an all-or-nothing process. This behavior gives rise to the characteristic sawtooth profile, as first described by Rief et al. [123]. Since fibronectin is composed of three different classes of subunits, differing mainly in the number of amino acids, the different events can be easily assigned by monitoring the unfolding forces and elongation lengths after bond rupture.
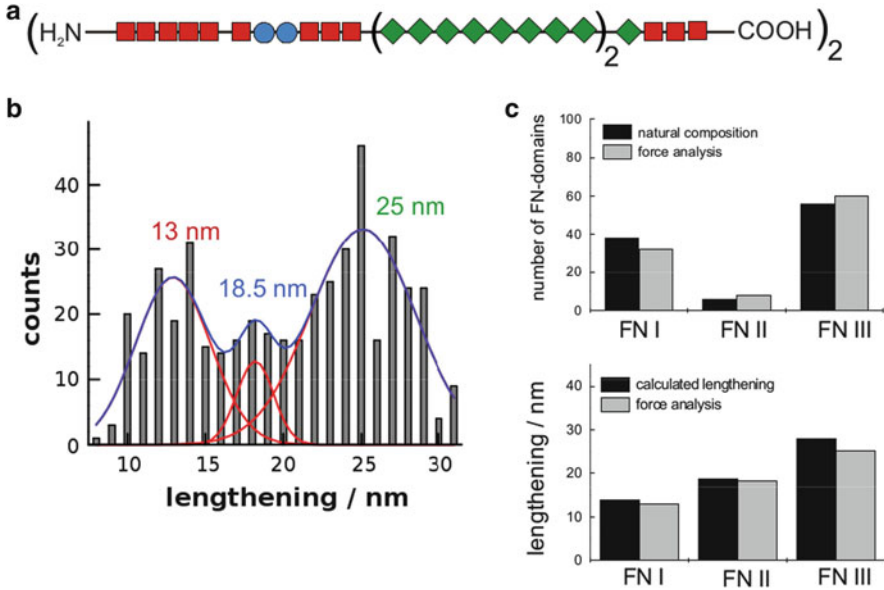
Fig. 27 (**a**) Structure of fibronectin composed of (■) FN-I (45 aa), (•) FN-II (60 aa), and (♦) FN-III (90 aa) domains. Cell binding to integrins is mainly provided by FN-III domains, which carry the RGD sequence, whereas attachment to collagen and fibrin is realized by FN-I subunits. (**b**) Histogram showing the lengthening of different domains due to subsequent unfolding of the modular filament fibronectin. Three Gaussian peaks were fitted to the data with peak maximums at 12.9 ± 0.6 nm representing FN-I, 18.2 ± 0.9 nm for FN-II, and 25.1 ± 0.5 nm for FN-III units. The integral of the corresponding Gaussian curves is related to the percentage of subunit occurrence in native fibronectin, i.e., 153.7 for FN-I, 38 for FN-II, and 280.5 events for FN-III subunits. (**c**) Statistical analysis of occurrence and lengthening, as obtained from force extension curves. Reproduced from [131] by permission of the PCCP Owner Societies

Of the three different domains, the FN-I domains possess the least amount of amino acids and hydrogen bonds and thus exhibit generally lower unfolding forces of about 50–100 pN, while showing an average lengthening of only about 13 nm (Fig. 27). FN-II domains are composed of 60 amino acids, thus showing intermediate unbinding forces and a lengthening of about 18.5 nm [127]. Figure 26 also shows the prominent unfolding events of FN-III domains, with an average lengthening of 25 nm and unfolding forces ranging from 100 to 200 pN depending on the number of units stretched and the overall compliance of the system. A higher compliance reduces the unfolding force. Notably, the unfolding force is a function of the contour length and therefore of the number of subunits between tip and substrate. Besides, the probability of bond breakage decreases with decreasing number of subunits between tip and sample and thereby displays smaller forces. Figure 27 summarizes the results from many pulling events and also shows a compilation of the expected and measured lengthening of each type of subunit and their occurrence. From structural data of native fibronectin, we expected to

Fig. 28 Unfolding force of
FN-III domains as a
function of domain number
and presence of ectoine.
Reproduced from [131] by
permission of the PCCP
Owner Societies
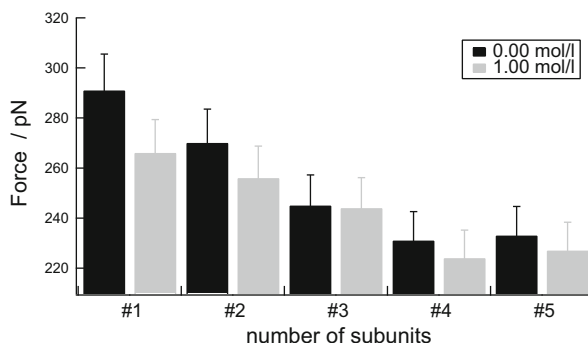
find a distribution showing three maxima. Fitting of three Gaussian curves to the
histogram data (Fig. 27b) results in domain lengthening corresponding well to
the expected changes in contour length for FN-I, FN-II, and FN-III domains.

Influence of Ectoine on the Unfolding Force of FN-III

The major question was whether bacterial osmolytes increase the stability of proteins
and nucleic acids by preferential exclusion of ectoine from the interface. First, we
investigated the influence of the presence of ectoine and sarcosine on the unfolding
force of the individual FN-III subunits of native fibronectin. After recording the
force–extension curves and quantifying the unfolding forces (as shown in Fig. 28),
we classified the unfolding forces according to their unfolding history (five groups)
and compiled the data in a histogram. The unbinding force decreases with increasing
number of folded domains between tip and sample, as expected from stochastics.
Although we accounted for the history of unfolding, no significant impact of ectoine
or sarcosine on the unfolding force was observed. Although differences in the
unfolding forces in the presence of osmolytes might be obscured by changes in the
persistence and contour length, it is conceivable that neither ectoine nor sarcosine
affect the inner structure of the protein domains but have larger impact on the whole
filament by compacting the structure, as expected from the interpretation following
Timosheff [110, 111, 117]. Thus, we concluded that the impact of osmolytes on the
compliance of the whole molecule should be more significant than on the unfolding
forces. Hence, we elucidated whether the tendency of the molecule to adopt a more
coiled structure is enhanced by the addition of compatible solutes.

In order to study the influence of bacterial osmolytes on the compliance of the
protein we described the force as a function of the extension by a conventional
WLC model. This model has provided reasonable results in many studies where the
Scanning Force Microscopy (SFM) or optical tweezers have been used to stretch
long proteins, even though it fails in some important situations (as discussed in

Fig. 29 Persistence length of fibronectin as a function of ectoine concentration. A lower persistence length implies a higher tendency to form coils. Reproduced from [131] by permission of the PCCP Owner Societies
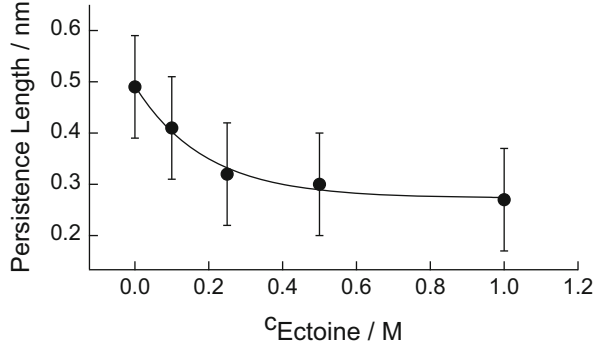
Sect. 1). Nevertheless, systematic shifts in molecular properties determined with the help of the WLC model remain correct, although the absolute values might be erroneous. The force is given by rearranging Eq. (2):

$$f = \frac{k_{\mathrm{B}}T}{l_{\mathrm{p}}} \left[\frac{1}{4} \left(1 - \frac{x}{L} \right)^{-2} + \frac{x}{L} - \frac{1}{4} \right] \tag{8}$$

The parameter of interest in the context of preferential exclusion is the persistence length l_{p} as a measure for the elasticity of the protein. Note that for a worm-like polymer $l_{\mathrm{p}} \sim \kappa R^4$, with κ being the bending modulus and R the radius of the cross-section of the filament. Higher values indicate a tendency to form more extended rod-like structures. For instance, the persistence length of double-stranded DNA is about 50 nm, whereas the persistence length of a single-stranded DNA or polypeptide is only about 0.5–1 nm. WLC fits were carried out for a large number of fibronectin molecules under different conditions. Figure 29 shows the mean persistence length as a function of the osmolyte (ectoine) concentration. The persistence length significantly decreases from 0.5 to 0.29 nm with increasing concentration of ectoine [131]. This implies that the tendency of the molecule to adopt a more condensed (i.e., coiled conformation) increases due to preferential exclusion of ectoine from the interface. Control experiments with sodium chloride at a high concentration of 4 M do not show any significant change in persistence length.

In conclusion, bacterial osmolytes such as ectoine and sarcosine stabilize extracellular matrix proteins, as revealed in mechanical single-molecule experiments, not by increasing intramolecular forces as one might expect but by thermodynamically forcing the molecule into a more compact structure and thus increasing the entropic spring constant of the molecule due to preferential exclusion of the corresponding osmolyte. The unfolding energy in the presence of ectoine increases accordingly.

3.2 Mechanically Interlocked Calix[4]arene Dimers Under External Force

Thermal fluctuations in macroscopic systems close to a local equilibrium are merely a source of noise that can usually be neglected in everyday physics. In contrast to macroscopic systems, small systems are largely influenced by thermal fluctuations. At macroscopic scales, the experimental outcomes are essentially independent of the repetition of thermodynamic manipulations following the identical protocol, but the situation is different at microscopic scales, where outcomes from repetitions of an identical experimental protocol vary substantially [133]. Recent theoretical developments in nonequilibrium physics have shown how, by using these fluctuations, it is possible to recover free energy differences and energy landscapes from experiments carried out far from equilibrium [104, 134–137]. The methods usually require large sampling of rather rare events, which poses a great challenge to experimentalists. Experiments suitable for verifying modern theories of nonequilibrium statistical mechanics like the fluctuation theorem and the Jarzynski relation need to fulfill two fundamental requirements [138]. On the one hand, manipulative devices such as optical/magnetic tweezers or force microscopes with a bendable cantilever are needed that allow fixing a single state variable such as a defined force or distance, while other variables are allowed to fluctuate [139]. Moreover, since sampling of rare events is necessary to obtain the free energy from out-of-equilibrium experiments, a large number of repetitions are required to reconstruct the underlying potential. Therefore, stable experimental set-ups and special molecules with defined states are needed to permit a large number of realizations with variable outcome.

Therefore, tunable model systems of sufficient smallness are required that can be subjected to defined external mechanical perturbations, giving access to both the equilibrium and nonequilibrium regimes. This allows verification of the free energy differences computed from nonequilibrium conditions by switching the system into quasi-equilibrium conditions, providing the free energy differences directly.

Although supramolecular assemblies are ideally suited to study the physics of small systems under external load, only a few are appropriate for the study of reversible and irreversible transformations. Most examples are from biomolecules such as proteins and nucleic acids [93, 140]. Along these lines, Bustamante and coworkers were the first to establish a reversible model system to apply Jarzynki's relation to compute the free energy difference from out-of-equilibrium experiments [141].

Recently, a supramolecular model system was successfully established that allows the assessment of different regimes of externally stimulated stochastic barrier crossing, ranging from quasi-equilibrium to nonequilibrium bond breakage. This has been achieved by creating a modular molecule that prevents irreversible bond rupture by mechanically limiting the separation distance using entangled loops (Fig. 30) [95]. The mechanical lock limits the distance of the two binding partners, raising
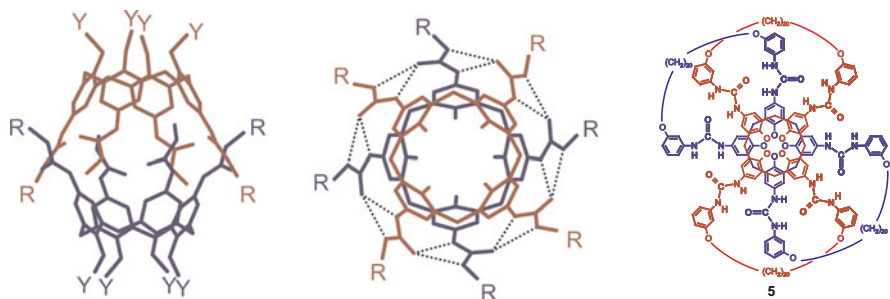
Fig. 30 A single nanocapsule consisting of two intramolecular entangled bis-loop tetra-urea calix [4]arenes. The dimer is connected by 16 hydrogen bridges, of which 8 are strong and 8 are weak. Reproduced with permission from [95]

the rebinding probability especially at low loading rates. Re-formation of dimeric capsules is observed even during separation. Oligomerization of the dimeric calix[4] arene catenanes provides an intrinsic control that single molecules have indeed been extended and that the observed rupture events correspond to individual breakage of the calixarene capsules. Essentially, we found that calixarene dimers separate under an external force ramp independently, but stochastically generate a characteristic sawtooth pattern. The rupture forces are velocity dependent and re-formation of hydrogen bonds is observable at low loading and relaxation rates. MD simulations in conjunction with stochastic modeling suggests that an intermediate structure arises due to steric reasons (vide infra).

3.2.1 Force Spectroscopy of Single bis-Loop Tetra-Urea Calix[4]arene Catenanes

Modular long-chain molecules can be stretched with different loading rates to study the unfolding and refolding of intramolecular hydrogen bonds in entangled bis-loop tetra-urea calix[4]arene catenanes.[1] One nanocapsule consists of two calixarene monomers, which are connected via 16 hydrogen bonds to form a dimer (Fig. 30). The hydrogen bridges are formed by four urea groups located at the upper ring of each calixarene monomer. Between two monomers, eight hydrogen bonds are classified as strong (N–O distance, 0.286 nm) and eight as weak (N–O distance, 0.329 nm) [143]. Together with the spacers, each bimolecular capsule exhibits a length of about 4 nm in the initial or unified state and approximately 6 nm in the elongated or ruptured state after the disjoining of intramolecular hydrogen bonds, as demonstrated by MD simulations (vide infra). The nanocapsules are oligomerized via covalent coupling between the amino and carboxyl

---

[1] This chapter contains and describes the results obtained in the framework of the Ph.D. thesis of Matthias Janke [142]. Figs. 30, 32, 33, 34, 35, 36, 37, 38, and 39 are taken from this work.
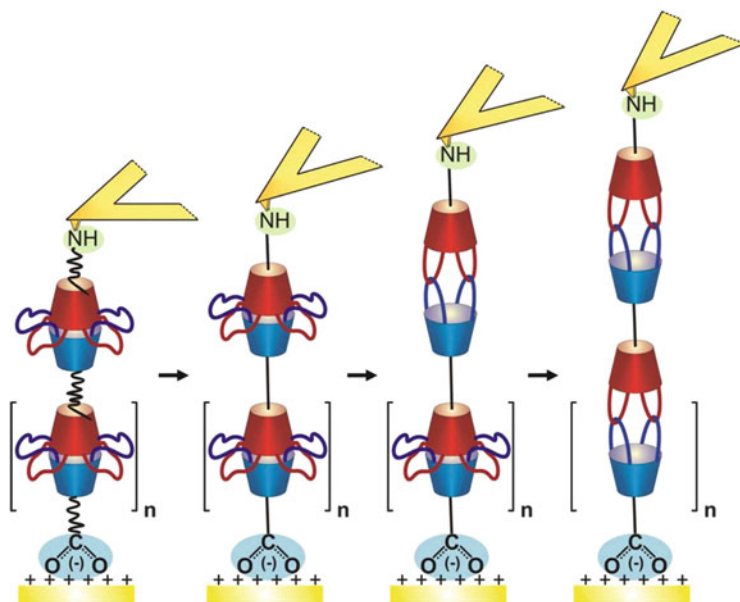
Fig. 31 Envisioned single-molecule stretching experiment involving oligomeric calixarene catenanes. The molecule is noncovalently attached to the (Trimethylammoniumundecanthiol) functionalized and thereby positively charged gold substrate via terminal carboxyl groups. By touching the surface with the functionalized tip, a molecule is randomly picked up by forming a covalent bond between the terminal amino group and the succinimidyl ester groups of the functionalized cantilevers. By increasing the distance from the surface, the molecule is continuously stretched until intramolecular breakage of the hydrogen bridges occurs. Reproduced with permission from [95]

groups, forming amide bonds located at the terminus of each spacer, resulting in long-chain molecules with four to six connected capsules on average. The relevant force scale in these experiments usually ranges between 10 and 150 pN. An illustration of the envisioned experiment is shown in Fig. 31.

Force–Extension Curves of Calixarene Catenane Oligomers

Stretching experiments with oligomerized calixarene catenanes exhibit a characteristic sawtooth pattern in which the individual rupture events are separated by merely 1–2 nm due to the presence of the mechanical lock provided by the entangled loops. Figure 32 shows two stretching curves from experiments carried out at different loading rates, together with corresponding elastic WLC fits to the data. A persistence length of about 0.4 nm is indicative of a single polymer chain such as a polypeptide or single-stranded DNA. The difference in the contour length ΔL mirrors the length extension between two successive rupture events and is a function of the loop length. The sawtooth pattern of the extension curves

Fig. 32 Stretching and subsequent rupturing of an individual oligo calixarene catenane at two different velocities: (**a**) 1,500 and (**b**) 30,000 pN/s. The *lines* represent worm-like chain (WLC) fits to the data with a persistence length l_p of approx. 0.4 nm. The changes in the contour length ΔL, as obtained from the fitting procedure, are of about 1–2 nm. These abrupt extensions represent the elongation of single capsules after breakage of the intramolecular hydrogen bonds, as illustrated in the *inset* of (**a**). The markers inside the tight capsule on the *left* represent intact hydrogen bridges
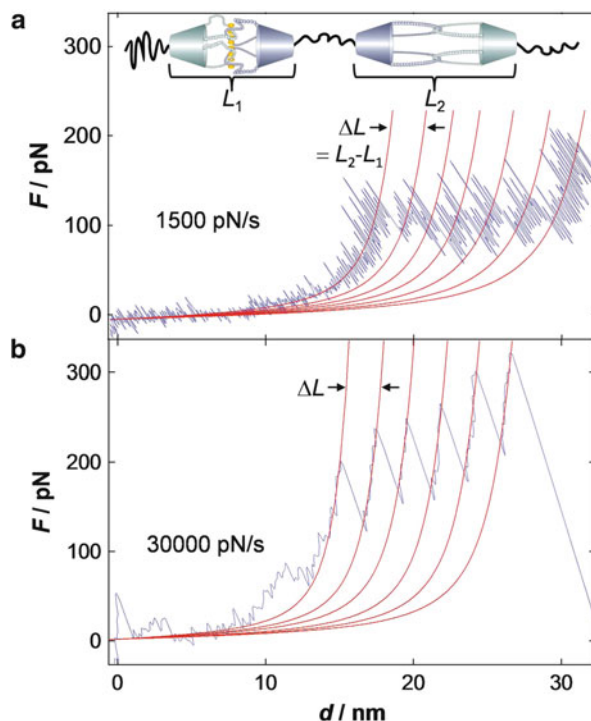
mirror independent breaking of individual capsules, similar to observations in the case of fibronectin. During a pulling experiment, the tension inside a long-chain molecule is identical throughout the entire contour length. An abrupt extension of the chain caused, e.g., by a sudden opening of one of its nanocapsules, leads to a rapid drop in tension. This release in tension is detected by the cantilever, which shows a sudden drop in deflection. The probability of capsule opening depends on the number n of available closed capsules prior to pulling and therefore decreases after elongation of each capsule. As a consequence, the subsequent rupture event occurs at larger force, as observed for unfolding of fibronectin or titin [123, 127]. The force of each subsequent rupture event rises with a factor of f_β/n, where f_β is the thermal activation parameter and n represents the number of previous ruptured bonds [132].

The number of capsules in between the substrate and the AFM tip can be directly counted from the number of events displayed in the stretching curve, e.g., in Fig. 32a six capsules are stretched and in Fig. 32b five capsules. This is in good agreement with the estimated number of capsules computed from the longest contour length, L (35 nm in Fig. 32a and 28.5 nm in Fig. 32b), divided by the theoretically expected length of an elongated capsule of about 6 nm. Therefore, it is safe to assume that all capsules break upon extension. Besides, the rupture forces rise with increasing loading rate, which is discussed in greater detail below.
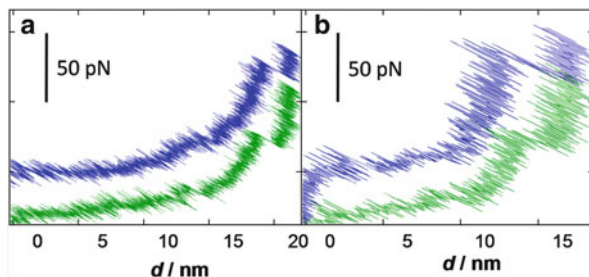
Fig. 33 Examples of force–distance curves showing distinct refolding events in the retracting curve (*green*). Measurements were carried out with a loading rate of (**a**) 60 and (**b**) 300 pN/s. On purpose, an offset of 30 pN was applied between trace (pulling, *blue*) and retrace (relaxation, *green*) to improve visibility

Reversibility of Pulling Experiments

Due to the mechanical lock provided by two entangled loops, the opening of the nanocapsules can be reversed because the two binding partners are not separated "infinitely" as in many other experiments involving single-molecule pulling. In contrast, the mechanical lock keeps the two capsules close together so that rebinding is a likely scenario. Thus, re-formation of hydrogen bridges is possible and rejoining of capsules should be observed in the retracting curves. An example of clearly visible rejoining events upon relaxation is shown Fig. 33. The hysteresis between pulling and relaxation increases with higher loading rates. As a consequence, assignable rejoining events of capsules are only found at lower pulling velocities. Importantly, the rebinding events are usually less clearly pronounced than the rupture events and therefore the retraction curve usually displays a less obvious sawtooth pattern. Stretching of a molecule frequently results in a separation from either the tip or the substrate, which prevents an investigation of rejoining events of the capsules. Successful stretching and relaxing cycles of a clamped single molecule are often called "fishing" experiments. Figure 34 displays a successful fishing experiment, in which the maximal stretching distance is increased gradually between the individual force curves until the molecule loses contact in force curve number 31.

In contrast to the force-induced unfolding of modular proteins such as titin, tenascin, spectrin, or fibronectin, the rupture events of calixarene dimers show no wear off, i.e., no reduction in the number of unfolding capsules in the subsequent stretching cycle. Interestingly, we found that even while pulling on the molecule, rejoining of previously separated capsules into intact tight capsules occurs. This has also been described by Schlierf and Rief for protein folding from and unfolding into an intermediate state [144]. Rejoining of the dimers is identifiable by a pronounced force plateau in the extension curves (Fig. 34, cycles 4 and 26–28). Such a plateau has also been described by Bustamante and coworkers for ribozyme unfolding and is found in MC simulations [145]. However, in contrast to the work of Bustamante, a substantial hysteresis between extension and relaxation of the oligomer remains in
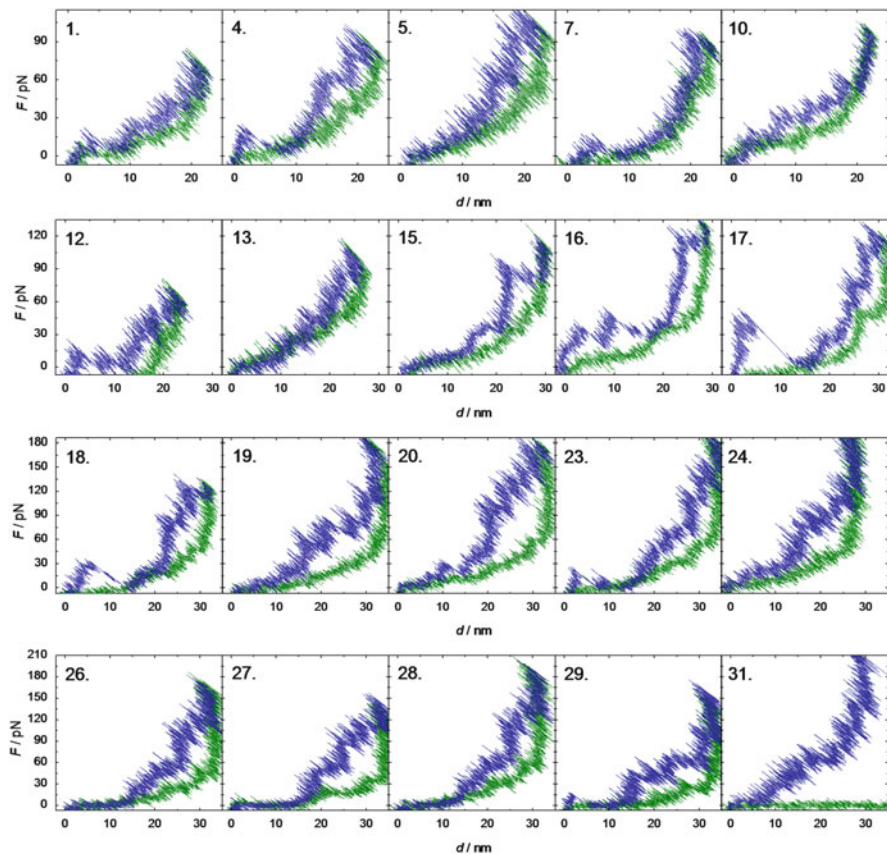
Fig. 34 Sequence of stretching (*upper traces*) and relaxing (*lower traces*) curves (*1–31*) of a single calixarene catenane oligomer at a loading and relaxing rate of 300 pN/s. The distance between tip and sample was gradually increased between each cycle, leading to higher forces. In *cycle 31* the molecule eventually lost contact with either the substrate or the cantilever. Note that rejoining of capsules during relation is frequently observed

our experiments, indicating that the system is still far from equilibrium at a loading rate of 300 pN/s. Information about the energy landscape of the 16 hydrogen bonds in a dimer can be obtained from velocity-dependent measurements supported by MD simulations and stochastic calculations (vide infra).

Analysis of the Force–Distance Curves

A comprehensive quantitative analysis of rupture and rejoining events of experiments with calixarene catenanes was carried out by identifying the force and extension of each rupture event, as well as the rejoining forces, and then compiling
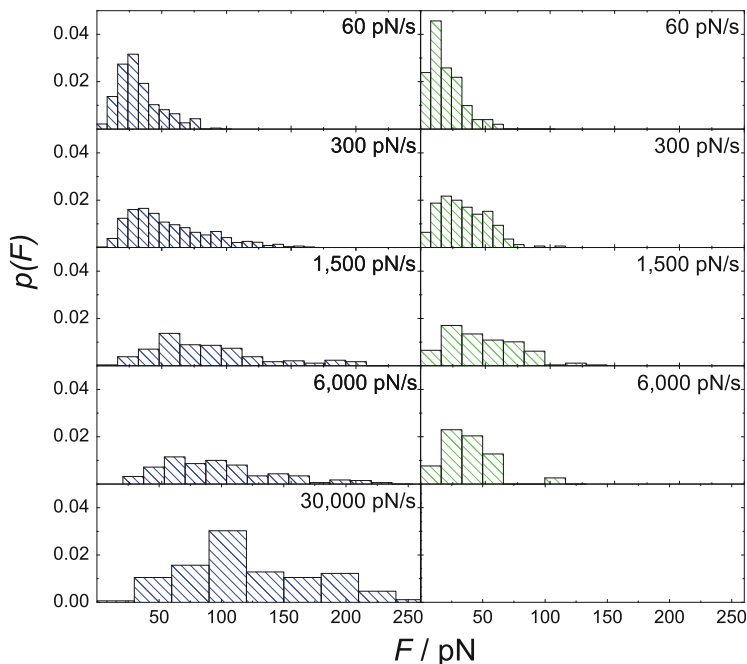
Fig. 35 Histograms of rupture force (*left*) and rejoining force (*right*) obtained at different loading rates (from *top* to *bottom*: 60, 300, 1,500, 6,000, and 30,000 pN/s)

the data in histograms. Figure 35 shows that the average rupture forces $\langle F_{rup} \rangle$ increase with loading rate and that the normalized rupture force histograms broaden significantly. In contrast, the mean rejoining forces $\langle F_{rejoin} \rangle$ decrease with increasing loading rate while the width broadens. Rejoining of capsules is no longer observed at loading rates larger than 6,000 pN/s, supporting the idea that the pulling process is irreversible. Figure 36 shows the distribution of ΔL obtained from rupture events as a function of the loading rate. Mostly, a bimodal distribution is apparent, especially at lower loading rates, where a lot of data could be acquired due to better measurement conditions. The maxima are located at around 1 and 2 nm, indicating the presence of a sufficiently stable intermediate. The appearance of such an intermediate state during pulling is also observed in MD simulations (vide infra) and has been considered and examined by stochastic modeling.

To determine a correlation between length extension and rupture force, all events are classified into a lengthening of about 1 (± 0.4) or 2 (± 0.4) nm. As expected, events with a capsule elongation of 2 nm exhibit slightly higher average rupture forces (Fig. 37).

Fig. 36 Histograms of the individual extensions ΔL_1, ΔL_2 found per rupture event as a function of loading rate by fitting two Gaussian functions to the data: (**a**) 60 pN/s, $\Delta L_1 = (1.2 \pm 0.49)$ nm, $\Delta L_2 = (2 \pm 0.66)$ nm; (**b**) 300 pN/s, $\Delta L_1 = (1.0 \pm 0.1)$ nm, $\Delta L_2 = (1.9 \pm 1.3)$ nm; (**c**) 1,500 pN/s, $\Delta L_1 = (1.2 \pm 0.58)$ nm, $\Delta L_2 = (2.1 \pm 0.33)$ nm; (**d**) 6,000 pN/s, $\Delta L_1 = m$ (0.9 ± 0.6) nm, $\Delta L_2 = (1.9 \pm 1.33)$ nm; (**e**) 30,000 pN/s, no data analysis possible
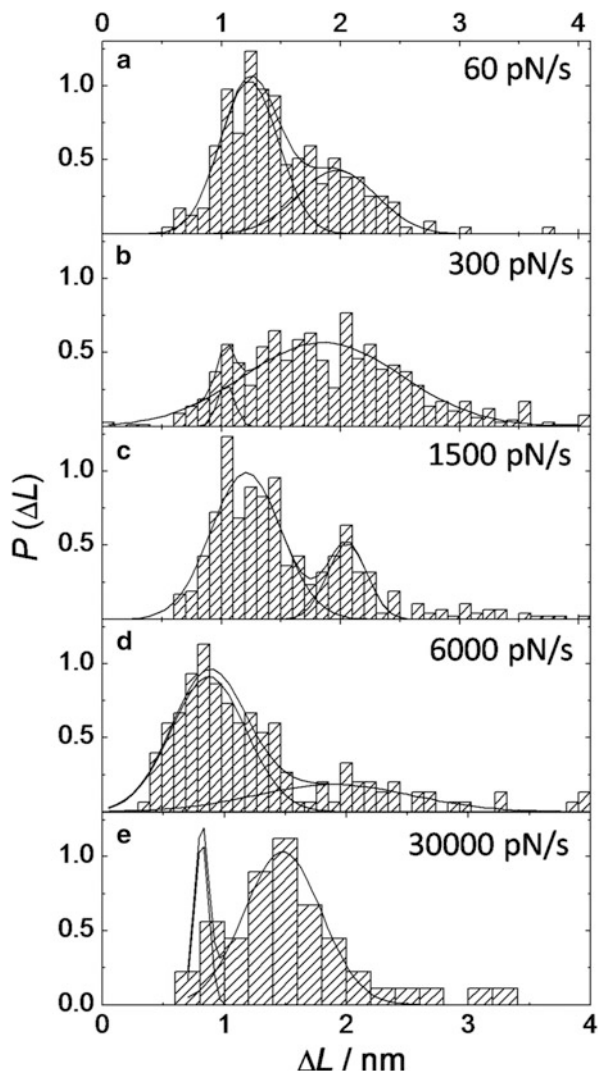
Impact of the Solvent on Rupture Forces

All force–distance experiments were conducted in mesitylene (1,3,5-trimethylbenzene) solution. Mesitylene is a good solvent for calixarenes and has a high boiling point, which is desirable for single-molecule experiments. The dimeric calixarene capsules have a cavity size suitable for the inclusion of solvent molecules such as mesitylene. Because hydrogen bridges inside the capsules can be influenced by the dielectric permittivity of the guest molecules, it is important to test whether impurities of the solvent may affect the experimental result. Toluene is probably the most likely contamination. Control experiments were conducted with 5 vol% toluene as an
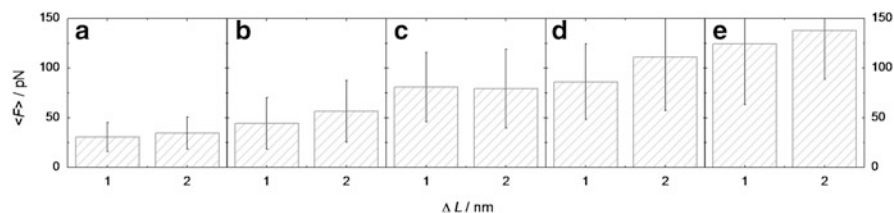
Fig. 37 Rupture forces corresponding to $\Delta L \approx 1$ nm and $\Delta L \approx 2$ nm as a function of loading rate: (**a**) 60, (**b**) 300, (**c**) 1,500, (**d**) 6,000, and (**e**) 30,000 pN/s. Generally, rupture forces increase with pulling velocity and differences in rupture forces become more distinct with higher loading rate
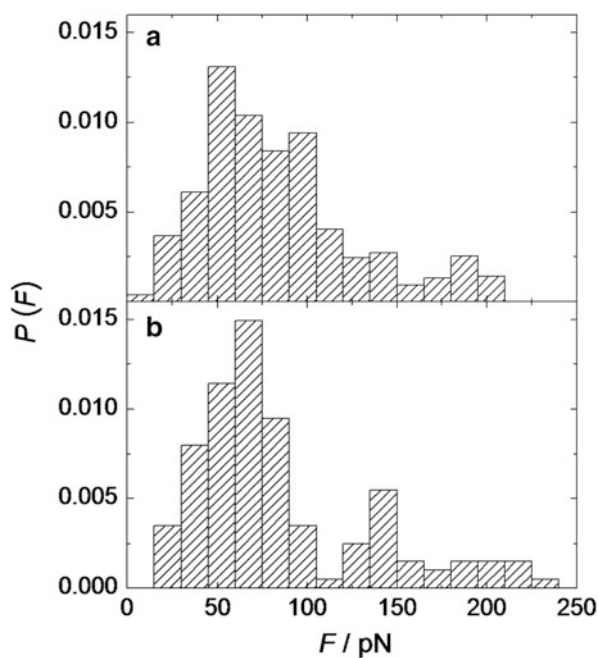
Fig. 38 Rupture force histograms (loading rate 1,500 pN/s) obtained in (**a**) pure mesitylene and (**b**) mesitylene with toluene (5 vol%) as an additive

additive. Figure 38 shows rupture force distributions for experiments carried out in pure mesitylene (Fig. 38a) and with 5 vol% toluene (Fig. 38b). The histograms are virtually identical, as expected, since mesitylene and toluene have the same dielectric constant ($\epsilon_r = 2.4$ at room temperature).
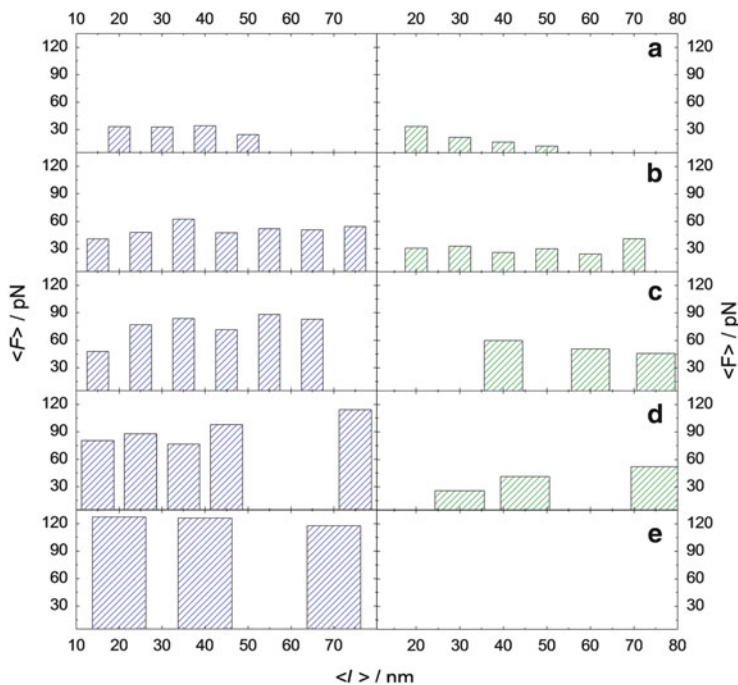
Fig. 39 Average rupture and rejoining forces (rupture, *left*; rejoining, *right*) as a function of contour length at different loading rates: (**a**) 60, (**b**) 300, (**c**) 1,500, (**d**) 6,000, and (**e**) 30,000 pN/s (no rejoining events are found)

Effect of the Linker and Contour Length on Capsule Breakage

The elastic response of a molecular system is directly coupled to the mechanical properties of the transducer. Evans and Ritchie studied the effect of a soft molecular linkage on the strength of a weak connecting bond [132]. Based on theoretical considerations, Friedsam et al. illustrated the effect of a soft spacer on rupture force histograms [146]. Due to the presence of polymer spacers with a certain length distribution, the rupture force histograms were broadened significantly. Thormann et al. investigated the impact of either a bovine serum albumin (BSA) linker or poly(ethylene)glycol (PEG) spacer on the well-known biotin–streptavidin bond [147]. In the case of the BSA linker, they observed a soft response of the BSA that leads to a broadening in the distribution of the rupture forces. The PEG linker causes a reduction in average unbinding forces in comparison to calculations without a soft spacer. Due to the soft linker, the force ramp inclines towards lower forces compared to a linear force ramp. Hence, the molecular system spends more time at low forces, which increases rupture probability at low forces.

If the molecules are rather stiff $\kappa_{\text{linker}} >> \kappa_{\text{c}}$, with κ_{c} denoting the stiffness of the transducer and κ_{linker} the stiffness of the linker, the rupture force is approximately independent of the molecule length and elastic properties, and the spring

constant of the cantilever dominates the force ramp in the experiment. Polymer linkers display a nonlinear compliance that requires more sophisticated treatment to correctly describe the elastic properties of the molecular chain. Figure 39 shows that no correlation between contour length and average forces was found experimentally. This is attributed to the considerably small length of the decylene ($C_{10}H_{20}$) spacers. Regardless of this finding, only molecules in a contour length interval of 10–30 nm were selected for further analysis to avoid unnecessary histogram broadening.

Comparison with Theory

The profound understanding of breakage and rebinding of hydrogen bridges under external load is a major goal in understanding the function of complex biological structures. Calix[4]arene catenanes are an ideally suited model system for studying reversible binding, experimentally with dynamic force spectroscopy (DFS) and theoretically by means of MD simulations (described in detail in Sect. 3.1).

Theories based on diffusive barrier crossing with a fluctuating cantilever assume either a one-well potential, when no rebinding is taken into account, or a two-well potential when rebinding is included [107–109, 148, 149]. Here, a similar approach was used to evaluate the rates of barrier crossing and location of barriers using stochastic models to capture the force spectra obtained experimentally. In order to extract relevant parameters from the energy landscape of the calixarene dimer, it is mandatory to first estimate the number of dominant states and barriers. The following scrutiny is based on data analysis recently published by Janke et al. [95]. First, it is instructive to analyze the increase in length ΔL of the molecule upon rupture, extracted from fitting a WLC function to the data as done before (vide supra) and compare this result, at least qualitatively, with MD simulations (Fig. 40a–c). Figure 40c shows a single pulling trajectory obtained from MD simulations displaying two distinct length jumps. The first sudden length increase can be attributed to H-bond breakage because it exceeds the typical reach of H-bonds (0.3 nm), and the second smaller sudden jump is assigned to the opening of an intermediate conformation. A more comprehensive study has been published by Schlesier et al. [98].

Both the experimentally obtained histogram (Fig. 40a) and the histogram compiling data from MD simulations (Fig. 40b) display the same bimodal distribution in ΔL centered at 1 and 2 nm, indicative of a intermediate state. The breakage of the H-bonds does not follow a specific sequence nor does it display the signature of cooperativity. It was found that the intermediate state was reasonably stable (>10 ns) in prolonged simulations at elevated temperature (460 K) under constant force. Possible conformations of the strained dimers captured by MD simulations at various times with the intermediate state at 1 ns are shown in Fig. 40d. Assignment of an intermediate state is often difficult and usually interfered indirectly from nonlinear force spectra [150]. A nonlinear relationship between $\langle F_{rup} \rangle$ and $\ln(dF/dt)$ does not necessarily imply the presence
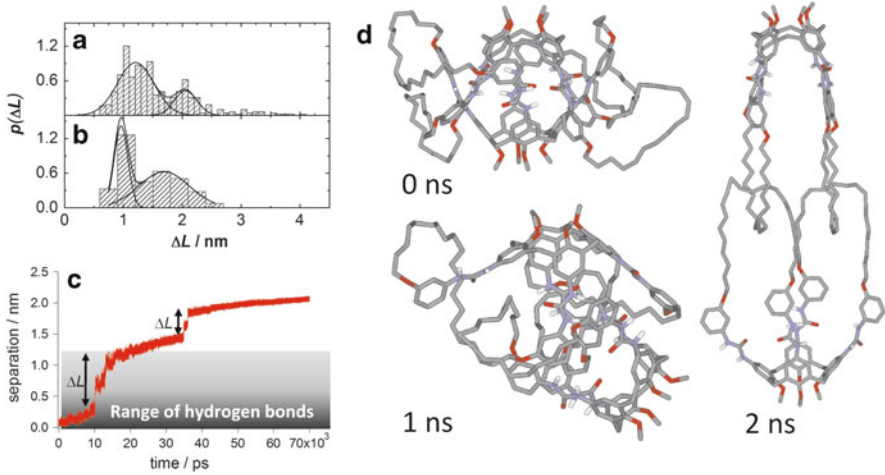
Fig. 40 Comparison of experimental results with MD simulations and stochastic modeling [95]. Histograms of dimer separation ΔL from (**a**) force experiments (1,500 pN/s) and (**b**) MD simulations. Fitting of two Gaussian functions to the corresponding histograms $p(\Delta L)$ provides mean separations ΔL at 1.2 ± 0.01 and 2.05 ± 0.02 nm for experimental force curves and 0.9 ± 0.14 and 1.7 ± 0.05 nm for MD simulations. (**c**) Separation of two calixarene monomers as a function of time, obtained from a single run. (**d**) Snapshots of a calix[4]arene dimer under harmonic load at various times. At 1 ns the intermediate state is shown. Reproduced with permission from [95]

of additional energy barriers, but could be rather a consequence of an intrinsic feature of diffusive barrier crossing with a fluctuating cantilever [149]. Figure 41a schematically shows the assumed energy potential with idealized cusp-like barriers. Stochastic analysis was carried out to propose parameters of a three-well-potential, such as the location of the energy barriers q_{TA} and q_{TB}, the position of the intermediate state q_I, the height of the energy barriers V_{TA} and V_{TB}, and the corresponding transition rates at zero force. Solution of the master equation provides the force-dependent populations of the corresponding states:

$$\frac{\mathrm{d}}{\mathrm{d}F} n_{\mathrm{x}}(F) = \left(\frac{\mathrm{d}F}{\mathrm{d}t}\right)^{-1} \left[-\sum_{Y(\neq X)} k_{XY}(F) n_X(F) + \sum_{Y(\neq X)} k_{XY}(F) n_Y \right] \qquad (9)$$

where $n_X(F)$ is used to provide approximate values for the aforementioned parameters of the three-well-potential. This can be accomplished by fitting the resulting probability distributions to the rupture and rejoining histograms recorded at different loading rates (Fig. 41b, c). Optimization of parameters provided locations for the first barrier at approximately $q_{TA} \approx 0.3$ nm and the second at $q_{TB} \approx 1.1$ nm. The probability densities $p(F)$ are plotted for a loading rate of 1,500 pN/s along with the experimental force histograms of rupture and rejoining forces. The rupture force histogram displays two clear maxima corresponding to
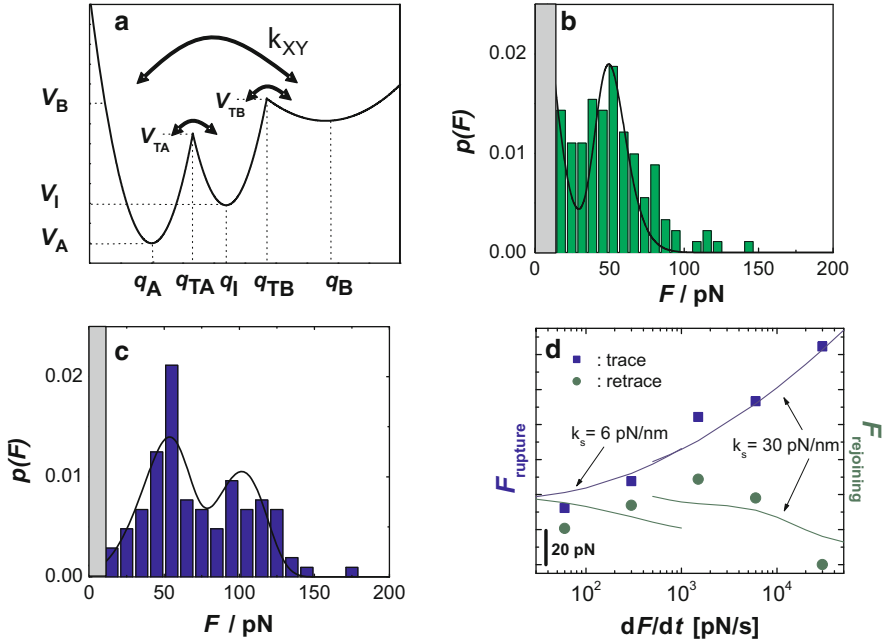
Fig. 41 Stochastic modeling of capsule breakage and rejoining suggests a three-well potential with a stable intermediate state. (**a**) Harmonic three-well potential centered at q_A, q_I, and q_B separated by two cusp-like barriers at q_{TA} and q_{TB}, with the corresponding rate constants at zero force $k_{XY}(0)$. Histograms of (**b**) rejoining force and (**c**) rupture force obtained at 1,500 pN/s, together with results from stochastic modeling (*lines*) in which the parameters of Eq. (9) were fitted to the data. The two clearly discernible peaks imply the presence of an intermediate. The *gray box* on the *left* indicates the force resolution due to thermal fluctuations of the cantilever. (**d**) Force spectrum showing mean rupture and rejoining forces computed from the histograms displayed in Fig. 35. The *blue lines* represent the mean rupture force obtained from stochastic modeling, and the *green lines* denote the mean rejoining forces. The *lines* are not continuous because two different cantilevers with force constants of 0.006 and 0.03 N/m were used. Reproduced with permission from [95]

the two barriers at q_{TA} and q_{TB}. Force spectroscopy data is shown in Fig. 41d. Mean rupture and rejoining forces are plotted as a function of loading rate on a semilogarithmic scale. Close to the equilibrium, rupture and rejoining forces converge to a constant force that is independent of the loading rate indicative of equilibrium conditions. A linear dependence of the average rupture force as a function of $\ln(dF/dt)$, as suggested by Bell, is only observed at high loading rates [103]. Because two different cantilever spring constants (0.006 and 0.03 N/m) were used, the curves are not continuous.

With the advent of nanotechnology, interest in the physics of small systems far from equilibrium has strongly increased. Suddenly, tiny systems in which thermal fluctuations prevail could be easily conceived and realized. Mechanically driven transformations, as carried out by single-molecule stretching experiments

or observed for molecular machines, offer a unique way to study fundamental theories of statistical mechanics associated with fluctuation-dissipation theorems. Here, we describe the mechanics of two modular polymers, i.e., fibronectin and oligomeric calix[4]arene catenanes under external force. Whereas fibronectin is a native protein that displays irreversible rupture of protein domains upon extension, the linked calix[4]arene catenanes allow re-formation of separated bonds on experimental time scales due to mechanical locks. In this context, two fundamental questions were addressed. First, to what extent can proteins be stabilized by exposure to compatible solutes and, second, can we investigate H-bond breakage both close to equilibrium and also far from equilibrium using a single molecule. We found that, addressing the first question, it is possible to drive the system into a more coiled conformation but not to enhance the stability of the domains. Preferential exclusion of compatible solutes such as ectoine forces the protein into a more globular conformation, which is displayed by a reduced persistence length. Calixarene catenanes mechanically arrest the system in close vicinity after rupture. The loops therefore permit the reversible rupture and rejoining of individual nanocapsules formed by the calix[4]arene catenanes. Addressing the second question, experiments carried out by force spectroscopy using an atomic force microscope in conjunction with MD simulations and stochastic modeling revealed the presence of an intermediate state between the closed and open state of a single nanocapsule. In summary, entangled nanocapsules are ideal model systems for investigating the strength of hydrogen bonds on a single molecule level with adjustable reversibility. Reversibility can be tuned by changing the loop length, as demonstrated by MD simulations. Longer loop lengths drive the system out of equilibrium by widening the potential, making rejoining highly improbable. The system offers the opportunity to study the energy landscape of a single (chemical) reaction as a function of molecular design and external force, making it an ideal test bed for modern theories of nonequilibrium statistical mechanics.

4 Mechanical Properties of Nucleic Acids with Binding Pockets for Small Molecules

Mechanical properties of biopolymers such as nucleic acids, in particular of DNA, have become of high interest in material science. As a programmable scaffold, biopolymers can be designed to self-assemble into a variety of two- and three-dimensional structures and thus form an interesting platform for bottom-up assembly of nanoscale structures [151]. In addition to structures that can be predicted and rationally designed by engineering standard interactions of the Watson–Crick type, nucleic acids can establish noncanonical interactions to form complicated three-dimensional structures, including catalytic pockets and high affinity binding pockets for small molecules. Although such binding pockets cannot yet be rationally

engineered, they can be obtained with high efficiency by applying a combinatorial technique termed SELEX. The products of SELEX are so-called aptamers, i.e., nucleic acids that bind to a given target with high affinity. Thus, identified aptamers hold great interest, e.g., in analytics, diagnostics, and potentially in material science. However, as opposed to canonical Watson–Crick-based DNA structures [152], their mechanical properties have hardly been investigated at all [153].

One particularly interesting problem in the context of aptamer science is the detection of the binding of small molecules to macromolecules, and the impact of binding on the mechanical properties of nucleic acid structures. Previous approaches to this problem suffer from the need to chemically alter either the macromolecule or the small molecule (hereafter called the "analyte") in order to allow proper detection. Because even the smallest alterations to the chemical structure of an analyte induce significant changes to its physicochemical properties, we have devised a new approach to measure the interaction of nucleic acid aptamers and small molecules by atomic force spectroscopy (AFS). The approach combines both of the above-mentioned structural features of DNA, fusing the structural domain of an aptamer to the faithfully hybridizing stretches of Watson–Crick helices. Rather than immobilizing the interaction partners in a traditional AFS experiment on opposing surfaces (i.e., an aptamer on the AFM tip and the small molecule on a substrate surface), we split an aptamer structure into two parts and equipped both halves with flanking regions that would recognize the respective other half by Watson–Crick base pairing. Neither half of the aptamer alone retains sufficient structure for binding the analyte; instead, the fully competent binding pocket is transiently generated during the short period of an AFS measurement cycle, in which both components are in spatial proximity. Measurements in the absence and in the presence of an analyte should then reveal whether this period is sufficiently long to allow detectable binding events. Previous experiments had shown that transient binding motifs could in principle be assembled from DNA strands in situ. Thus, binding of a third DNA strand to a transient double-stranded DNA, as well as binding of intercalating small molecules to such a triple helix, could indeed be detected by force spectroscopy [154, 155]. As binding resulted in an increase of the most probable rupture force in each case, this was also anticipated for the new aptamer approach. However, it was entirely unclear whether the rather complicated binding pockets would form in a fast and reproducible manner, and whether the binding of a single analyte molecule would be strong enough to be detectable.

For a proof of concept, we used a DNA aptamer that binds adenosine monophosphate (AMP) [156]. The sequence of the DNA aptamer was 3-ACT GGAAGGAGGAGATGC-GCATCTAGGAGGTCCAGT-5 and provided two binding pockets (underlined bases) for AMP. The structure suggests a contribution of base stacking as well as of a total of five H-bonds to the binding derived from NMR analysis [157]. Furthermore, the aptamer structure is symmetric and thus provides binding pockets for two molecules of AMP, whose binding is highly cooperative [157, 158]. For the force spectroscopy measurements, the DNA sequence was split symmetrically in length between C–G. Then, the split sequences were equipped with a poly-A tail at the 5-ends, a six-carbon spacer to
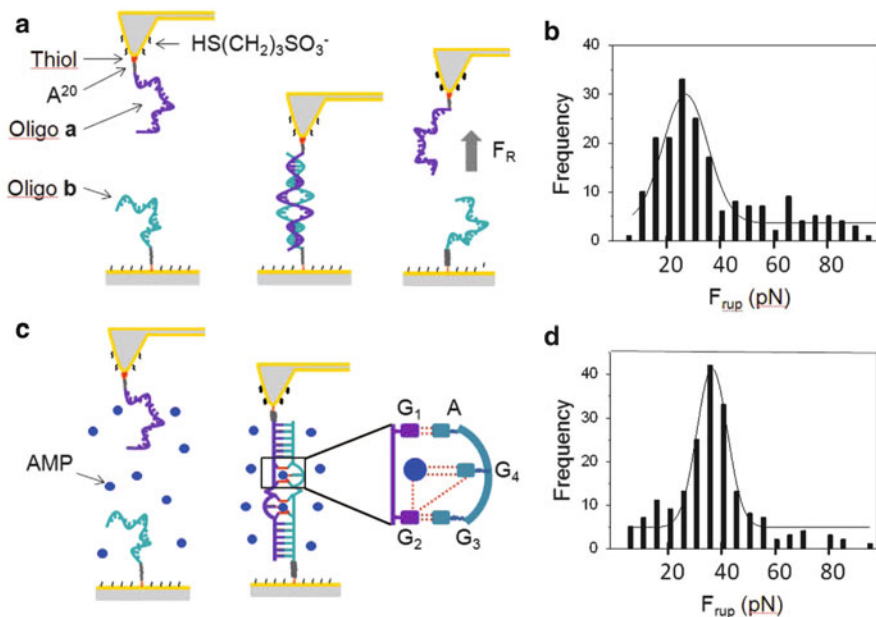
Fig. 42 (**a**) Outline of the split AMP aptamer experiment. The adhesion force between the AFS tip and the sample surface was minimized by the additional immobilization of $HS(CH_2)_3SO_3Na$. Both parts of the oligonucleotide aptamer (oligo-a and oligo-b) were immobilized by thiol linkers to the gold-coated tip and sample surface, respectively. Upon withdrawal of the tip away from the surface at a speed of 400 nm/s the rupture force F_{rup} was measured. Force–distance curves were repeated 1,000 times. (**b**) Plot of the measured rupture forces in a histogram. The fit of the data with a Gaussian distribution leads to the most probable rupture force, here 27.3 ± 8.4 pN. For the Gaussian fit we have ignored rupture forces >40 pN. (**c**) When AMP target molecules were added to the buffer solution, AMP molecules entered the binding pockets and eight additional hydrogen bonds were formed at each pocket (*dotted lines*). (**d**) In the presence of AMP, the most probable rupture force was 38.8 ± 5.2 pN. Reprinted with permission from [156]. Copyright (2011) American Chemical Society

allow for enough flexibility and sufficient spatial distance from the surface, and a terminal thiol group for immobilization on a Au surface. One strand was immobilized on the AFS tip (oligo-a, 3-ACTGGA-AGGAGG-AGATGC-A20-SH-5) and the other strand was immobilized on the substrate (oligo-b, 5-SH-A20-TGACCT-GGAGGA-TCTACG-3) (Fig. 42a, left). Now, upon moving the AFS tip close to the sample surface, oligo-a and oligo-b can partial hybridize and the binding pockets form (Fig. 42a, center). In the absence of AMP, a most probable force F_{rup} of 27 pN at a pulling speed of 400 nm/s between both oligonucleotides was measured (Fig. 42b). This rupture force was associated with the H-bonds formed by 12 base pairs in the hybridized system and was consistent with the measurements of Strunz et al. [152] under comparable conditions. When the buffer solution was changed to a buffer containing AMP (Fig. 42c), the analyte molecules could enter the binding pockets. At a concentration of 100 μM, which

is much greater than K_d of the target molecule AMP, we found an increase in the most probable rupture force to 39 pN (Fig. 42d). The increase in rupture force can be associated with 16 additional hydrogen bonds, i.e., eight additional hydrogen bonds per binding pocket (dotted lines in Fig. 42c, right). Then, the target molecule AMP was washed away by rinsing with pure buffer solution. The most probable rupture force returned to the values corresponding to the initial experiment in buffer, within the given experimental error. We concluded that the increase in rupture force was due to binding of AMP molecules to the transiently formed binding pockets of the bipartite aptamer.

The approach of splitting the aptamer sequences into a bipartite structure should be widely applicable for the detection of various small molecules, even cocaine [159, 160]. In order to prove the universality of the concept we used a DNA aptamer (sequence CCCTCTGGGTGAAGTAACTTCCATAATAGGAACAGAGGG) that binds cocaine via a hydrophobic pocket formed by a noncanonical three-way junction [161]. Splitting this sequence into complementary parts results in an asymmetric length of the oligonucleotides (oligo-a, 5-HS-A20AATAGGAACAGAGGG-3 and oligo-b, 5-HS-A20-CCCTCTGGGTGAAGTAACTTCCAT-3). Preliminary data from AFS experiments performed in a similar way to the experiments outlined above revealed most probable rupture forces of 40 ± 14 pN in the absence and 62 ± 19 pN in the presence of cocaine (Fig. 43). However, these measurements showed that only 60% of the rupture events can be associated with a cocaine molecule bound into the binding pocket. Thus, either formation of the binding pocket during measurement of the force–distance curve was hindered or the dissociation constant of this bipartite system deviated significantly from the literature value of 100 μM.

In general, the split aptamer concept enables us to study concentration dependencies of the target molecules. Thus, the binding constants of the target and the split aptamer systems as well as the selectivity of molecular interactions are accessible on a single-molecule level. In order to investigate whether the dissociation constant of the split systems differs from that of the non-split, ideal aptamer we have performed rupture force experiments using concentrations ranging from 0.01 to 100 μM [156]. For each concentration we have analyzed the corresponding histograms by fitting simultaneously two Gaussian distributions to the peaks corresponding to only oligo hybridization and to AMP binding, respectively. We found that with increasing concentration of AMP, the peak corresponding to AMP binding became more pronounced, i.e., more rupture events at higher forces were present. Simultaneously, the peak corresponding to only oligo hybridization was composed of fewer rupture events. At a concentration of 3.7 ± 2.5 μM, we observed the same amount of events. Thus, there is a 50% probability that AMP was bound in the binding pockets formed by the split aptamer at this concentration. Therefore, this concentration was attributed to the dissociation constant of the AMP binding aptamer. This value, which was obtained on a single-molecule level, is in agreement with a measurement performed by ultrafiltration (6 ± 3 μM) [164].
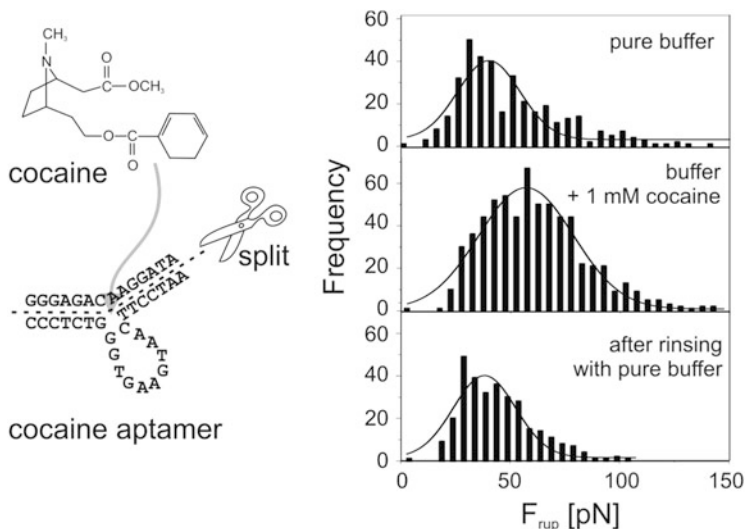
Fig. 43 *Left*: The split aptamer concept applied to the detection of cocaine. The binding constant of the cocaine–aptamer complex is approximately 100 μM [162]. The *line* indicates the split of the aptamer resulting in two oligos. *Right*: Histograms display the results performed in pure buffer solution (*top*), with 1 mM cocaine in the buffer solution (*middle*), and after rinsing cocaine away with pure buffer (*bottom*). Each set of data was fitted with a Gaussian distribution. Data adapted from the PhD thesis of Huong Nguyen [163]

In summary, our approach has established a number of highly interesting new findings for DNA aptamers. In addition to the proof-of-principle demonstration that binding of single analyte molecules alters the force spectra of split aptamers to a significant degree, we have developed the split aptamer concept into a generally applicable tool. Interesting open questions include the expansion to the RNA world with its huge variety of different and more complex three-dimensional structures. Investigation of the RNA aptamer, optimized for tetracycline binding [165], would be the first step into transferring the knowledge we acquired.

References

1. Lavery R, Lebrun A, Allemand J-F, Bensimon D, Croquette V (2002) J Phys Condens Matter 14:R383
2. Strick TR, Dessinges M-N, Charvin G, Dekker NH, Allemand J-F, Bensimon D, Croquette V (2003) Rep Prog Phys 66:1–45
3. Gallyamov MO (2011) Macromol Rapid Comm 32:1210
4. Binder K, Paul W, Strauch T, Rampf F, Ivanov V, Luettmer-Strathmann J (2008) J Phys Condens Matter 20:494215
5. Luettmer-Strathmann J, Rampf F, Paul W, Binder K (2008) J Chem Phys 128:064903
6. Rampf F, Paul W, Binder K (2005) Europhys Lett 70:628

7. Binder K, Baschnagel J, Müller M, Paul W, Rampf F (2006) Macromol Symp 237:128
8. Rampf F, Binder K, Paul W (2006) J Polym Sci B Polym Phys 44:2542
9. Paul W, Strauch T, Rampf F, Binder K (2007) Phys Rev E 75:060801(R)
10. Paul W, Rampf F, Strauch T, Binder K (2007) Macromol Symp 252:1
11. Paul W, Rampf F, Strauch T, Binder K (2008) Comput Phys Commun 179:17
12. Taylor MP, Paul W, Binder K (2009) Phys Rev E 79:050801(R)
13. Taylor MP, Paul W, Binder K (2009) J Chem Phys 131:114907
14. Taylor MP, Paul W, Binder K (2010) Phys Procedia 4:151
15. DeGennes P-G (1979) Scaling concepts in polymer physics. Cornell University Press, Ithaca
16. Ivanov VA, Paul W, Binder K (1998) J Chem Phys 109:5659
17. Grassberger P (1997) Phys Rev E 56:3682
18. Hsu H-P, Grassberger P (2011) J Stat Phys 144:597
19. Kratky O, Porod G (1949) J Colloid Sci 4:35
20. Hsu H-P, Paul W, Binder K (2012) J Chem Phys 137:174902
21. Schaefer DW, Joanny JF, Pincus P (1980) Macromolecules 13:1280
22. Hsu H-P, Binder K (2012) J Chem Phys 136:024901
23. Norisuye T, Fujita H (1982) Polym J 14:143
24. Pincus P (1976) Macromolecules 9:386
25. Saleh OA, McIntosh DB, Pincus P, Ribeck N (2009) Phys Rev Lett 102:068301
26. Binder K, Butt H-J, Floudas G, Frey H, Hsu H-P, Landfester K, Kolb U, Kühnle A, Maskos M, Müllen K, Paul W, Schmidt M, Spiess HW, Virnau P Structure formation of polymeric building blocks: complex polymer architectures. Adv Polym Sci, in press doi:10.1007/12_2013_230
27. Eisenriegler E, Kremer K, Binder K (1982) J Chem Phys 77:6296
28. Eisenriegler E (1993) Polymers near surfaces. World Scientific, Singapore
29. Descas R, Sommer J-U, Blumen A (2004) J Chem Phys 120:8831
30. Grassberger P (2005) J Phys A Math Gen 38:323
31. Bhattacharya S, Rostiashvili VG, Milchev A, Vilgis TA (2009) Macromolecules 42:2236
32. Klushin LI, Polotsky AA, Hsu H-P, Markelow DA, Binder K, Skvortsov AM (2013) Phys Rev E 87:022604
33. DeGennes P-G (1976) J Phys (France) 37:1445
34. Hsu H-P, Binder K (2013) Macromolecules 46:2496
35. Birshtein TM, Zhulina EB, Skvortsov AM (1979) Biopolymers 18:1171
36. Corsi A, Milchev A, Rostiashvili VG, Vilgis TA (2005) J Chem Phys 122:094907
37. Rother G, Findenegg GF (1998) Colloid Polym Sci 276:496
38. Omarjee P, Hoerner P, Riess G, Cabuil V, Mondain-Monval O (2001) Eur Phys J E 4:45
39. Taubert A, Napoli A, Meier W (2004) Curr Opin Chem Biol 8:598
40. Sommer JU, Daoud M (1995) Europhys Lett 32:407
41. Chatellier X, Joanny J-F (2000) Eur Phys J E 1:9
42. Lyatskaya Y, Gersappe D, Gross NA, Balazs AC (1996) J Chem Phys 100:1449
43. Chen ZY (1999) J Chem Phys 111:5603
44. Chen ZY (2000) J Chem Phys 112:8665
45. Corsi A, Milchev A, Rostiashvili VG, Vilgis TA (2006) Europhys Lett 73:204
46. Corsi A, Milchev A, Rostiashvili VG, Vilgis TA (2006) Macromolecules 39:1234
47. Corsi A, Milchev A, Rostiashvili VG, Vilgis TA (2006) J Polym Sci B 44:2572
48. Corsi A, Milchev A, Rostiashvili VG, Vilgis TA (2006) Macromolecules 39:7117
49. de Gennes P-G (1987) Adv Coll Int Sci 27:189
50. Fleer GJ, Scheutjens JMHM, Cohen-Stuart TCMA, Vincent B (1993) Polymers at interface. Chapman and Hall, London
51. Milchev A, Binder K (1996) Macromolecules 29:343
52. Bhattacharya S, Hsu H-P, Milchev A, Rostiashvili VG, Vilgis TA (2008) Macromolecules 41:2920

53. Bhattacharya S, Milchev A, Rostiashvili VG, Grosberg AY, Vilgis TA (2008) Phys Rev E 77:061603
54. Strick T, Allemand J-F, Croquette V, Bensimon D (2001) Phys Today 54:46
55. Celestini F, Frisch T, Oyharcabal X (2008) Phys Rev E 70:012801
56. Kikuchi H, Yokoyama N, Kajiyama T (1997) Chem Lett 11:1107
57. Rief M, Oersterhelt F, Heymann B, Gaub HE (1997) Science 275:1295
58. Smith SB, Cui Y, Bustamante C (1996) Science 271:795
59. Kafri Y, Mukamel D, Peliti L (2002) Eur Phys J B 27:135
60. Bhattacharya S, Milchev A, Rostiashvili VG, Vilgis TA (2009) Phys Rev E 79:030802 (R)
61. Milchev A, Rostiashvili VG, Bhattacharya S, Vilgis TA (2011). Polymer chain adsorption on a solid surface: scaling arguments and computer simulations. In: Michailov M (ed) Nanophenomena at surfaces. Springer series in surface sciences, vol 47. Springer, Berlin Heidelberg, p 185
62. Bhattacharya S, Milchev A, Rostiashvili VG, Vilgis TA (2009) Eur Phys J E 29:285
63. Skvortsov AM, Klushin LI, Birshtein TM (2009) Polym Sci A (Moscow) A 51:1
64. Paturej J, Milchev A, Rostiashvili VG, Vilgis TA (2012) Macromolecules 45:4371
65. Dimitrov DI, Klushin L, Milchev A, Binder K (2008) Phys Fluids 20:092102
66. Milchev A, Klushin L, Skvortsov A, Binder K (2010) Macromolecules 43:6877
67. Meller A (2003) J Phys Condens Matter 15:R581
68. Milchev A (2011) J Phys Condens Matter 23:103101
69. Nakane JJ, Akeson M, Marziali A (2003) J Phys Condens Matter 15:R1365
70. Meller A, Nivon L, Branton D (2001) Phys Rev Lett 86:3435
71. Kasianowicz JJ, Brandin E, Branton D, Deamer DW (1996) Proc Natl Acad Sci USA 93:13770
72. Slonkina E, Kolomeisky AB (2003) J Chem Phys 118:7112
73. Wei D, Yang W, Jin X, Liao Q (2007) J Chem Phys 126:204901
74. Milchev A, Binder K, Bhattacharya A (2004) J Chem Phys 121:6042
75. Milchev A, Binder K (2005) Computer Phys Commun 169:107
76. Slatex GW, Guo HL, Nixon GI (1997) Phys Rev Lett 78:1170
77. Dubbeldam JLA, Milchev A, Rostiashvili VG, Vilgis TA (2007) Phys Rev E 76:010801 (R)
78. Dubbeldam JLA, Milchev A, Rostiashvili VG, Vilgis TA (2007) Eurphys Lett 79:18002
79. Dubbeldam JLA, Milchev A, Rostiashvili VG, Vilgis TA (2009) J Phys Condens Matter 21:098001
80. Dubbeldam JLA, Milchev A, Rostiashvili VG, Vilgis TA (2009) Ann N Y Acad Sci 1161:95
81. Sung W, Park PJ (1996) Phys Rev Lett 77:783
82. Muthukumar M (1999) J Chem Phys 111:10371
83. Bhattacharya A, Morrison WH, Luo K, Ala-Nissll T, Ying S-C, Milchev A, Binder K (2009) Eur Phys J E 29:423
84. Bhattacharya A, Binder K (2010) Phys Rev E81:041804
85. Sakaue T (2007) Phys Rev E 76:021803
86. Sakaue T (2010) Phys Rev E 81:041808
87. Dubbeldam JLA, Rostiashvili VG, Milchev A, Vilgis TA (2011) Phys Rev E 83:011802
88. Dubbeldam JLA, Rostiashvili VG, Milchev A, Vilgis TA (2013) Phys Rev E 87:032147
89. Dubbeldam JLA, Rostiashvili VG, Milchev A, Vilgis TA (2012) Phys Rev E 85:041801
90. Chatelain C, Kantor Y, Kardar M (2008) Phys Rev E 78:021129
91. Storm AJ, Storm C, Chen J, Zandbergen H, Joanny J-F, Dekker C (2005) Nano Lett 5:1193
92. Klushin LI, Skvortsov AM, Hsu H-P, Binder K (2008) Macromolecules 41:5890
93. Liphardt J, Onoa B, Smith S, Tinoco I, Bustamante C (2001) Science 292:733
94. Gebhardt JCM, Bornschlögl T, Rief M (2010) Proc Natl Acad Sci USA 107:2013
95. Janke M, Rudzevich Y, Molokanova O, Metzroth T, Mey I, Diezemann G, Marszalek PE, Gauss J, Böhmer V, Janshoff A (2009) Nat Nanotechnol 4:225
96. Sauvage J-P, Dietrich-Buchecker C (1999) Molecular catenanes, rotaxanes, and knots. Wiley-VCH, Weinheim

97. Wang L, Vyotsky M, Bogdan A, Bolte M, Böhmer V (2004) Science 304:1312
98. Schlesier T, Metzroth T, Jahnshoff A, Gauss J, Diezemann G (2011) J Phys Chem B 115:6445
99. Oostenbrink C, Villa A, Mark AE, van Gunsteren WF (2004) J Comput Chem 25:1656
100. Schlesier T, Diezemann G (2013) J Phys Chem B 117:1862
101. Jorgensen WL, Maxwell DS, Tirado-Rives J (1996) J Am Chem Soc 118:11225
102. Cornell WD et al (1995) J Am Chem Soc 117:5179
103. Bell GI (1978) Science 200:618
104. Dudko OK, Hummer G, Szabo A (2008) Proc Natl Acad Sci USA 105:15755
105. Seifert U (2002) Europhys Lett 58:792
106. Li F, Leckband D (2006) J Chem Phys 125:194702
107. Diezemann G, Janshoff A (2008) J Chem Phys 129:084904
108. Diezemann G, Schlesier T, Geil B, Janshoff A (2010) Phys Rev E 82:051132
109. Diezemann G, Janshoff A (2009) J Chem Phys 130:041101
110. Arakawa T, Timasheff SN (1983) Arch Biochem Biophys 224:169
111. Arakawa T, Timasheff SN (1985) Biophys J 47:411
112. Yancey PH, Clark ME, Hand SC, Bowlus RD, Somero GN (1982) Science 217:1214
113. Santoro MM, Liu Y, Khan SMA, Hou LX, Bolen DW (1992) Biochemistry-US 31:5278
114. Galinski EA, Pfeiffer H-P, Trüper HG (1985) Eur J Biochem 149:135
115. Galinski EA (1995) Adv Microb Physiol 37:273
116. Knapp S, Ladenstein R, Galinski EA (1999) Extremophiles 3:191
117. Timasheff SN (1992) In water and life. Springer, Berlin
118. Janshoff A, Neitzert M, Oberdörfer Y, Fuchs H (2000) Angew Chem Int Ed 39:3212
119. Bizzarri AR, Cannistraro S (2010) Chem Soc Rev 39:734
120. Puchner EM, Gaub HE (2009) Curr Opin Struct Biol 19:605
121. Fisher TE, Carrion-Vazquez M, Oberhauser AF, Li H, Marszalek PE, Fernandez JM (2000) Neuron 27:435
122. Noy A (ed) (2008) Handbook of molecular force spectroscopy. Springer, Berlin
123. Rief M, Gautel M, Oesterhelt F, Fernandez JM, Gaub HE (1997) Science 276:1109
124. Rief M, Grubmüller H (2002) ChemPhysChem 3:255
125. Oberhauser AF, Marszalek PE, Erickson HP, Fernandez JM (1998) Nature 393:181
126. Rief M, Pascual J, Saraste M, Gaub HE (1999) J Mol Biol 286:553
127. Oberdörfer Y, Fuchs H, Janshoff A (2000) Langmuir 16:9955
128. Müller DJ, Baumeister W, Engel A (1999) Proc Natl Acad Sci USA 96:13170
129. Kedrov A, Janovjak H, Sapra KT, Müller DJ (2007) Annu Rev Biophys Biomol Struct 36:233
130. Yamada KM (1983) Annu Rev Biochem 52:761
131. Oberdörfer Y, Schrot S, Fuchs H, Galinski E, Janshoff A (2003) Phys Chem Chem Phys 5:1876
132. Evans E, Ritchie K (1999) Biophys J 76:2439
133. Bustamante C, Liphardt J, Ritort F (2005) Phys Today 58:43 doi:10.1063/1.2012462
134. Hummer G, Szabo A (2010) Proc Natl Acad Sci USA 107:21441
135. Hummer G, Szabo A (2001) Proc Natl Acad Sci USA 98:3658
136. Crooks GE (2000) Phys Rev E 61:2361
137. Jarzynski C (1997) Phys Rev Lett 78:2690
138. Harris NC, Song Y, Kiang C-H (2007) Phys Rev Lett 99:068101
139. Neuman KC, Nagy A (2008) Nat Methods 5:491
140. Stigler J, Ziegler F, Gieseke A, Gebhardt JCM, Rief M (2011) Sci Signal 334:512
141. Alemany A, Ribezzi-Crivellari M, Ritort F (2013) Recent progress in fluctuation theorems and free energy recovery. In: Klages R, Just W, Jarzynski C, Schuster HG (eds) Nonequilibrium statistical physics of small systems: fluctuation relations and beyond. Wiley-VCH, Weinheim, p 155
142. Janke M (2008) Atomic force microscopy of biomimetic systems. Ph.D. thesis, Mainz
143. Vysotsky MO, Bolte M, Thondorf I, Bšhmer V (2003) Chem Eur J 9:3375

144. Schlierf M, Rief M (2005) J Mol Biol 354:497
145. Onoa B, Dumont S, Liphardt J, Smith SB, Tinoco I, Bustamante C (2003) Science 299:1892
146. Friedsam C, Wehle AK, KŸhner F, Gaub HE (2003) J Phys Condens Matter 15:S1709
147. Thormann E, Hansen PL, Simonsen AC, Mouritsen OG (2006) Colloids Surf B 53:149
148. Lee G, Khadar A, Yong J, Peter A, Vann B, Marszalek PE (2006) Proc Natl Acad Sci USA 104:20719
149. Hummer G, Szabo A (2003) Biophys J 85:5
150. Merkel R, Nassoy P, Leung A, Ritchie K, Evans E (1999) Nature 397:50
151. Rothemund PWK (2006) Nature 440:297
152. Strunz T, Oroszlan K, Schafer R, Guntherodt HJ (1999) Proc Natl Acad Sci USA 96:11277
153. Neupane K, Yu H, Foster DA, Wang F, Woodside MT (2011) Nucleic Acids Res 39:7677
154. Ling L, Butt HJ, Berger R (2004) J Am Chem Soc 126:13992
155. Ling L, Butt H-J, Berger R (2006) Appl Phys Lett 89:113902
156. Nguyen T-H, Steinbock L, Butt HJ, Helm M, Berger R (2011) J Am Chem Soc 133:2025
157. Lin CH, Patel D (1997) J Chem Biol 4:817
158. Nonin-Lecomte S, Lin HC, Patel JD (2001) Biophys J 81:3422
159. Baker BR, Lai RY, Wood MS, Doctor EH, Heeger AJ, Plaxco KWJ (2006) J Am Chem Soc 128:3138
160. Liu J, Lu Y (2006) Angew Chem Int Ed 45:90
161. Neves MAD, Reinstein O, Saad M, Johnson PE (2010) Biophys Chem 153:9
162. Swensen JS, Xiao Y, Ferguson BS, Lubin AA, Lai RY, Heeger AJ, Plaxco KW, Soh HT (2009) J Am Chem Soc 131:4262
163. Nguyen T-H (2013) Rupture forces of split aptamers. Ph.D. thesis, Mainz
164. Niazi JH, Lee SJ, Kim YS, Gu MB (2008) Bioorg Med Chem 16:1254
165. Müller M, Weigand JE, Weichenrieder O, Suess B (2006) Nucleic Acids Res 34:2607